EARTH SURFACE PROCESSES AND LANDFORMS
Earth Surf. Process. Landforms (2018)

Published online in Wiley Online Library
(wileyonlinelibrary.com) DOI: 10.1002/esp.4495

Particle transport mechanics and induced seismic noise in steep flume experiments with accelerometer-embedded tracers

Florent Gimbert,[1,2]* Brian M. Fuller,[2] Michael P. Lamb,[2] Victor C. Tsai[2] and Joel P. L. Johnson[3]
[1] Université Grenoble Alpes, CNRS, IGE, 38000 Grenoble, France
[2] Division of Geological and Planetary Sciences, California Institute of Technology, Pasadena, CA 91125, USA
[3] Department of Geological Sciences, University of Texas at Austin, Austin, TX 78712, USA

Received 29 November 2017; Revised 14 August 2018; Accepted 20 August 2018

*Correspondence to: Florent Gimbert, Université Grenoble Alpes, CNRS, IGE, 38000 Grenoble, France. E-mail: florent.gimbert@cnrs.fr; florent.gimbert@univ-grenoble-alpes.fr

ESPL
Earth Surface Processes and Landforms

ABSTRACT: Recent advances in fluvial seismology have provided solid observational and theoretical evidence that near-river seismic ground motion may be used to monitor and quantify coarse sediment transport. However, inversions of sediment transport rates from seismic observations have not been fully tested against independent measurements, and thus have unknown but potentially large uncertainties. In the present study, we provide the first robust test of existing theory by conducting dedicated sediment transport experiments in a flume laboratory under fully turbulent and rough flow conditions. We monitor grain-scale physics with the use of 'smart rocks' that consist of accelerometers embedded into manufactured rocks, and we quantitatively link bedload mechanics and seismic observations under various prescribed flow and sediment transport conditions. From our grain-scale observations, we find that bedload grain hop times are widely distributed, with impacts being on average much more frequent than predicted by existing saltation models. Impact velocities are observed to be a linear function of average downstream cobble velocities, and both velocities show a bed-slope dependency that is not represented in existing saltation models. Incorporating these effects in an improved bedload-induced seismic noise model allows sediment flux to be inverted from seismic noise within a factor of two uncertainty. This result holds over nearly two orders of magnitude of prescribed sediment fluxes with different sediment sizes and channel-bed slopes, and particle–particle collisions observed at the highest investigated rates are found to have negligible effect on the generated seismic power. These results support the applicability of the seismic-inversion framework to mountain rivers, although further experiments remain to be conducted at sediment transport near transport capacity. © 2018 John Wiley & Sons, Ltd.

KEYWORDS: river, bedload, seismology, laboratory, experiments, mechanics

Introduction

Recent studies have demonstrated that high-frequency (1–50 Hz) river-induced ground vibrations can be used to monitor key physical processes in rivers such as bedload sediment transport (Govi *et al.*, 1993; Burtin *et al.*, 2008; Tsai *et al.*, 2012; Cook *et al.*, 2018) and turbulent fluid flow (Schmandt *et al.*, 2013; Gimbert *et al.*, 2014). Of central interest is the sensitivity of near-river seismic observations to bedload transport, in particular bedload transport rates that control river morphology and erosion rates but remain challenging to measure directly (Garcia *et al.*, 2000; Rickenmann *et al.*, 2012; Lamb *et al.*, 2015; Whipple *et al.*, 2000; Cook *et al.*, 2013). Seismic waves generated by single-grain impacts are often not distinguishable in seismic records, but the integrated contribution of impacts from all transported grains generates sufficient ground motion energy to be detectable (Burtin *et al.*, 2008; Burtin *et al.*, 2011; Hsu *et al.*, 2011; Schmandt *et al.*, 2013; Roth *et al.*, 2014; Díaz *et al.*, 2014; Gimbert *et al.*, 2016). Although turbulent fluid flow also generates seismic noise (Schmandt *et al.*, 2013; Gimbert *et al.*, 2014; Gimbert *et al.*, 2016; Roth *et al.*, 2017), previous theory and its application at a natural scale suggest that the bedload and turbulent flow sources may be distinguished by analyzing ground motion at various frequencies and river-to-station distances (Gimbert *et al.*, 2014; Cook *et al.*, 2018). Seismic instrumentation offers the advantage of being relatively straightforward and low cost, potentially allowing more and larger rivers to be safely instrumented with minimal environmental perturbation.

To establish seismology as a robust observational means of quantifying bedload fluxes, a reliable mechanistic framework linking bedload mechanics to seismic ground motion is needed. Tsai *et al.* (2012) theoretically related grain impacts on the river bed to bedload-induced seismic signal characteristics. However, inversions of sediment flux using this framework (Tsai *et al.*, 2012; Chao *et al.*, 2015; Schmandt *et al.*, 2017) have not been tested and validated against independent transport measurements and may have large uncertainties due to the idealized bedload physics. In particular, Tsai *et al.*

(2012) described the kinematics of bedload transport as saltating grains interacting only with the river bed (and not with other transported grains) through vertical, elastic impacts that, for a given grain size and hydrological condition, occur at constant rate and strength. In reality, grains interact with each other and impact the bed intermittently with periods of saltation, rest, rolling or sliding (e.g., Lajeunesse *et al.*, 2010), which could bias predictions and inversions.

The primary goal of this study is to test the Tsai *et al.* (2012) model using flume experiments. Based on our detailed observations of grain-scale impacts, we also propose new physical descriptions that better capture bedload physics and evaluate accuracy of bedload flux inversions from seismic noise.

In the next section we first provide a brief background and new theoretical developments for modeling bedload-induced seismic noise. The experimental setup and methods are presented in the third section. In the fourth section we show experimental results, seismic power model predictions and bedload flux inversions. Finally, interpretations and implications for field applications are discussed in the fifth section.

Rationale

Theoretical model of Tsai et al. (2012)

Seismic ground motion power is commonly evaluated at location $\mathbf{x}$ and frequency f from the power spectral density (PSD) $P(f, \mathbf{x})$ of ground velocity time series $U(t, \mathbf{x})$ defined as

$$P(f, \mathbf{x}) = \frac{U(f, \mathbf{x})^2}{T} \tag{1}$$

where $U(f) = \int_0^T U(t) e^{-2\pi i f t} \mathrm{d}t$ is the Fourier transform of $U(t)$ over a time window of duration T. Note that here we use the notation U for ground velocity whereas Tsai *et al.* (2012) used $\dot{u}$ for it. From a given force time series $F(t, D, \mathbf{x}_0)$ applied by a grain of diameter D impacting the ground at location $\mathbf{x}_0$ in the channel, one can write (Aki and Richards, 2002)

$$U(f, D, \mathbf{x}) = F(f, D, \mathbf{x}_0) G(f, \mathbf{x}; \mathbf{x}_0) \tag{2}$$

where $G(t)$ is the velocity Green's function, $F(f, D, \mathbf{x}_0)$ and $G(f, \mathbf{x}; \mathbf{x}_0)$ are the Fourier transforms of $F(t)$ and $G(t)$, respectively.

Tsai *et al.* (2012) described $F(t)$ and $G(t)$ under multiple simplifying assumptions. First, Tsai *et al.* (2012) assumed that transported grains only impact the bed and not each other (see Figure 1a), and that impacts occur randomly in time; i.e. they are uncorrelated with each other. In this case, the source force power increases linearly with the number of grains. Second, Tsai *et al.* (2012) assumed that grains impact the river bed vertically (i.e. along direction 2; Figure 1b). In this case, $G(t)$ for surface waves reduces to $G_R(t)$ for Rayleigh waves, and hop times and impact velocities used to determine the vertical force time series $F_2(t)$ can be obtained from grain hop height and settling velocity, which are parameters commonly inferred from and calibrated using flume experiments (Sklar and Dietrich, 2004; Lamb *et al.*, 2008b; Chatanantavet *et al.*, 2013). Third, Tsai *et al.* (2012) assumed that grains of similar grain size exhibit an idealized saltation trajectory (e.g. no rolling or sliding) defined by single, constant values for hop time and impact velocity. These values were inferred from previous studies in which data averaging was conducted over multiple measurements (Sklar and Dietrich, 2004; Lamb *et al.*, 2008a). Thus the force time series defined in Tsai *et al.* (2012) is also an average quantity, which we denote by $\bar{F}_2(t)$, where

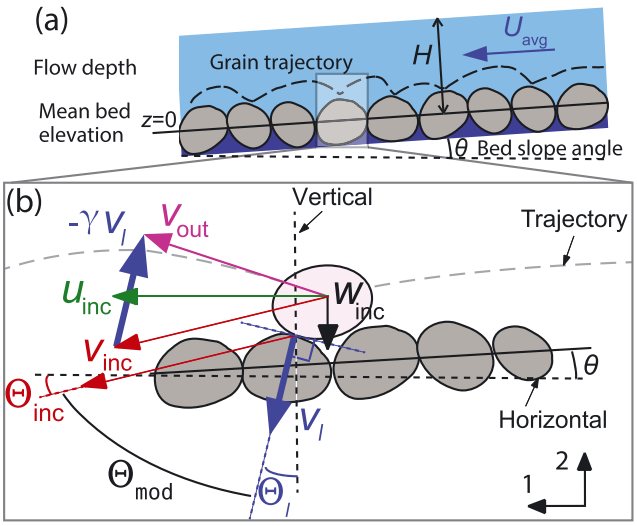

Figure 1. Sketch of (a) a typical bedload transport saltation trajectory and (b) the different velocities and angles involved in a moving grain impacting a rough river bed. U_{avg} is the depth-averaged stream-wise flow velocity (excluding subsurface flow). v_{inc} is the incident impact velocity vector (with horizontal component u_{inc} and vertical component w_{inc}), respectively, and oriented at an angle Θ_{inc} with respect to horizontal. v_I is the impact velocity vector oriented normal to local bed roughness, and oriented at an angle Θ_I with respect to vertical. v_{out} is the reflected velocity vector, and corresponds to the vectorial sum of v_{inc} with γv_I (using $\gamma = 1.13$). Θ_{mod} is the modified impact angle. [Colour figure can be viewed at wileyonlinelibrary.com]

the overbar indicates the average. Under these three simplifying assumptions, they were able to predict the total PSD $P^{\mathrm{Tsai}}(f, \mathbf{x})$ of vertical ground motion defined in Equation (1) by integrating seismic power due to $U(f, D, \mathbf{x})$ (Equation (2)) over the full size distribution of bedload transported grains $p_D(D)$ and along the full length of river R as

$$\begin{aligned} P^{\mathrm{Tsai}}(f, \mathbf{x}) &= \int_R \bar{F}_2^2(f, \mathbf{x}_0) G_{R,2}^2(f, \mathbf{x}; \mathbf{x}_0) \mathrm{d}\mathbf{x}_0 \\ \text{with} \quad \bar{F}_2^2(f, \mathbf{x}_0) &= \int_D \frac{n_D}{\bar{t}_I} \bar{F}_{I,2}^2(f, D, \mathbf{x}_0) \mathrm{d}D \end{aligned} \tag{3}$$

where $G_{R,2}(f, \mathbf{x}; \mathbf{x}_0)$ is the vertical-to-vertical velocity Green's function for Rayleigh waves, $\bar{F}_{I,2}(f, D, \mathbf{x}_0)$ is the single, average vertical impact force spectrum for a grain of diameter D, and $n_D(D) = p_D(D)N/L$ is the number of moving grains per unit grain size and per unit river length (with units m^{-2}), with N being the total number of sediment grains moving over length L and $\bar{t}_I(D)$ the average hop time between impacts of grains of diameter D. $\bar{F}_{I,2}(f, D)$ was calculated from the incident, average vertical velocity $\bar{w}_{inc}$ by assuming that the impact contact time t_c (~1 ms) is significantly shorter than $1/f_{max}$ where $f_{max} \approx 50$ Hz is the maximum investigated seismic frequency. (Here we use the notation $\bar{w}_{inc}$ for the incident, average vertical velocity whereas Tsai et al., 2012, used w_i for it.) In this case, $\bar{F}_{I,2}(f, D)$ has a flat amplitude spectrum set by momentum change as

$$\bar{F}_{I,2}(f, D) = I = m \int_0^{t_c} a(t) \mathrm{d}t = m(\bar{w}_{inc} + \bar{w}_{ref}) = \gamma m \bar{w}_{inc} \tag{4}$$

where I is the vertical impulse imparted by the impact, m is the mass of the impacting grain, $a(t)$ is the acceleration time series during an impact and $\bar{w}_{ref}$ is the reflected, average vertical impact velocity. $\gamma = 1 + e$ is a constant equal to 1 if the impact is perfectly inelastic ($w_{ref} = 0$) and 2 if

the impact is perfectly elastic ($w_{\text{ref}} = w_{\text{inc}}$). Tsai *et al.* (2012) assumed $\gamma = 2$ for simplicity. e is the restitution coefficient (Gondret *et al.*, 2002). Final model predictions using sediment flux q_b as the main control parameter were made by expressing the number n_D of moving grains of diameter D in Equation (3) as $n_D = q_{bD}W/(Vu_S)$, where u_S is the average stream-wise bedload velocity, W is the river width, V is the grain volume and $q_{bD} = p_D(D)q_b$ is sediment flux per unit grain size and per unit length.

Extension of the theory to a probabilistic framework with impacts on a rough river bed

We extend the theory of Tsai *et al.* (2012) to a probabilistic framework (including rolling or sliding, for example) that incorporates the full distributions of impact hop times t_l and velocities w_{inc} as opposed to simply average values $\bar{t}_l$ and $\bar{w}_{\text{inc}}$ as in Tsai *et al.* (2012). We describe seismic power P in the vertical component of ground motion from a probabilistic framework by defining the probability density function $p_l(t_l)$ of hop times between impacts and replacing Equation (3) from Tsai *et al.* (2012) by

$$P(f,\mathbf{x}) = \int_R \int_D \int_{t_l} P_{D,t_l}(f, D, t_l, \mathbf{x}; \mathbf{x}_0)\mathrm{d}t_l\,\mathrm{d}D\,\mathrm{d}\mathbf{x}_0$$
$$\text{where } P_{D,t_l}(f, D, t_l, \mathbf{x}; \mathbf{x}_0) = p_l(t_l)\frac{n_D}{t_l}F^2_{l,2}(f, D, t_l, \mathbf{x}_0)G^2_{R,2}(f, \mathbf{x}; \mathbf{x}_0) \tag{5}$$

where $F_{l,2}(f, D, t_l, \mathbf{x}_0) = \gamma m w_{\text{inc}}$ is the single vertical impact force spectrum for a grain of diameter D and a given impact hop time t_l. Deviations of predictions using this probabilistic scenario compared to the average one used in Tsai *et al.* (2012) can be quantified through the impact efficiency parameter $E_l(D)$ defined by comparing P in Equation (5) with P^{Tsai} in Equation (3) as

$$E_l(D) = \frac{\int_{t_l} p_l(t_l)\frac{n_D}{t_l}F^2_{l,2}(f, D, t_l, \mathbf{x}_0)\mathrm{d}t_l}{\frac{n_D}{\bar{t}_l}\bar{F}^2_{l,2}(f, D, \mathbf{x}_0)}. \tag{6}$$

Later we use the impact efficiency parameter $E_l(D)$ to quantify the control of bedload impact rate and velocity statistics on seismic noise power.

We further rewrite the theory of Tsai *et al.* (2012) for non-vertical impacts in a two-dimensional space. To do so, we consider two-dimensional impact force time series $F_{l,j}(t)$, where index $j = 1, 2$ stands for the horizontal (1) and vertical (2) directions (Figure 1b). Since Rayleigh waves are the only surface waves that contribute to seismic power in the vertical component of ground motion, we define the Green's function $G_{R,j}(t, \mathbf{x}; \mathbf{x}_0)$ as the vertical ground velocity at $\mathbf{x}$ due to an instantaneous force applied along direction j at $\mathbf{x}_0$. (One could also use the other horizontal components, although Love waves and a dependency of seismic power on source-to-station azimuth should be accounted for in that case). With these definitions, we obtain

$$P(f,\mathbf{x}) = \int_R \int_D \int_{t_l} \sum_{j=1}^{2} p_l(t_l)\frac{n_D}{t_l} \times F^2_{l,j}(f, D, t_l, \mathbf{x}_0)G^2_{R,j}(f, \mathbf{x}; \mathbf{x}_0)\mathrm{d}t_l\,\mathrm{d}D\,\mathrm{d}\mathbf{x}_0 \tag{7}$$

where $F_{l,j}(f, D, t_l, \mathbf{x}_0) = \gamma m v_{l,j}(t_l)$ and $v_{l,j}$, for a rough bed, is the jth component of the impact velocity vector oriented normal to local bed roughness (no friction; see Figure 1b). This definition for the impact velocity that generates seismic ground motion thus differs from that previously used in Tsai *et al.* (2012), which is strictly only appropriate for a smooth bed. Below, though, we show that smart rock data suggest that the assumption of vertical impacts is reasonable. Assuming that impacts are approximately vertical in natural settings, the vertical-to-vertical Green's function $G_{R,2}$ may be used and $F_{l,2}(f, D, t_i, \mathbf{x}_0)$ in Equation (7) becomes $F_{l,2}(f, D, t_i, \mathbf{x}_0) = \gamma m v_l(D, t_l, \mathbf{x}_0)$, where $v_l = \sqrt{v^2_{l,1} + v^2_{l,2}}$ is the norm of the impact velocity normal to the bed roughness approximated as $v_l \approx v_{l,2}$. Given an empirical expression for the impact efficiency parameter E_l (Equation (6)), Equation (7) simplifies to

$$P(f,\mathbf{x}) \approx \int_R \int_D E_l(D)P_D(f, D, \mathbf{x}; \mathbf{x}_0)\mathrm{d}D\,\mathrm{d}\mathbf{x}_0 \tag{8}$$

with $P_D(f)$ calculated as

$$P_D(f, D, \mathbf{x}; \mathbf{x}_0) = \frac{n_D}{\bar{t}_l}\bar{F}^2_{l,2}(f, D, \mathbf{x}_0)G^2_{R,2}(f, \mathbf{x}; \mathbf{x}_0) \tag{9}$$

with $\bar{F}_{l,2}(f, D, \mathbf{x}_0) = \gamma m \bar{v}_l(f, D, \mathbf{x}_0)$. Predictions using this improved modeling framework are ultimately compared with those using the original model of Tsai *et al.* (2012) on the basis of the experiments described below.

Experimental Strategy, Methods and Measurements

Experimental strategy to test the models

To conduct our experiments we use a ground-detached steel flume (Figure 2; see next subsection for details) that allows for varying flow (slope, discharge) and bedload transport conditions, but prevents us from evaluating seismic wave propagation (the Green's function $G(t)$; see Equation (2)) under natural conditions. We thus empirically measure the flume Green's function $G_F(t)$ using known forces applied to the flume bed, and focus our analysis on evaluating the bedload source force $F(t)$ and its control on bedload-induced seismic flume vibrations. The main components of the force $F(t)$ such as impact characteristics (mainly impact time and restitution coefficient; see Equation (4)) and bedload transport kinematics (mainly grain hop times and impact velocities) are inferred from the analysis of tracers referred to as 'smart rocks', which consist of three-component accelerometers embedded in aluminium housings with typical river grain geometries (Figure 2b; see also Olinde and Johnson (2015), and 'Smart rock calibration, methods and experimental plan' below). We then use these grain-scale observations to constrain the modeling of $F(t)$ by accounting for the full distributions of bedload hop times $p_l(t_l)$ and associated impact forces (see Equation (5)). Predictions of seismic noise using our grain-scale calibrated model are compared with seismic noise observed using a seismometer placed on the flume armature (see 'Seismic noise measurements' below).

Flume setup and transport conditions

Experiments were conducted in a 15 m long, 1 m wide tilting flume at the California Institute of Technology (Figure 2a). The setup of the flume is identical to that described in Lamb et al. (2017a, 2017b), and is briefly described here. The flume bed is made out of natural river cobbles with a median grain diameter of 4.5 cm glued to the steel floor in a layer of about one grain diameter thick. The average bed elevation measured by laser scan was 28 mm above the metal floor. Subsurface flow is

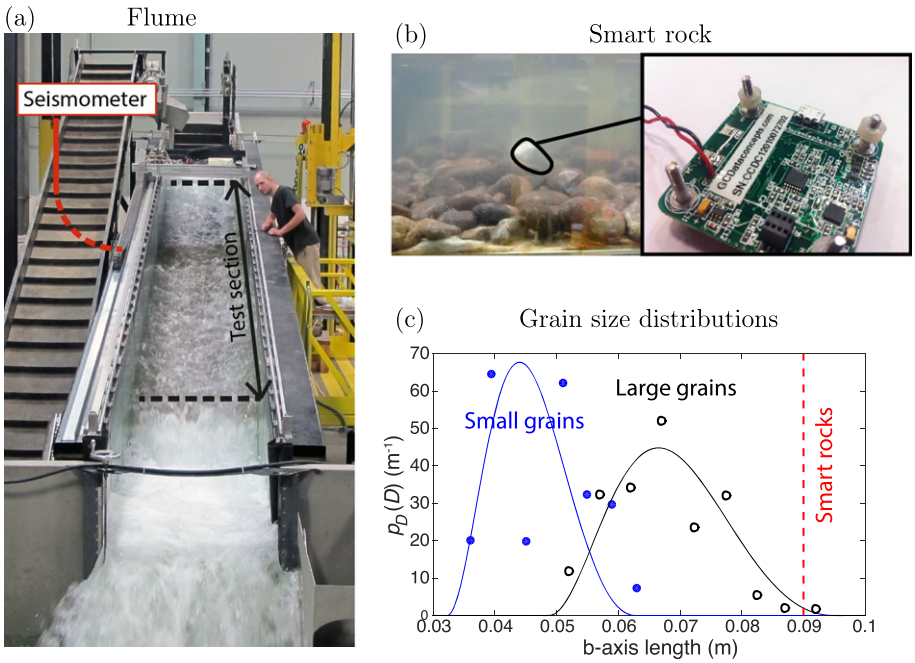

Figure 2. Experimental setup. (a) Picture of the flume with flowing water. (b) Picture of the smart rock resting on the flume cobble bed (left, see steel gray rock) and of the accelerometer device placed inside the rock (right). (c) Measured (circles) and fit (solid lines) grain size probability density function $p_D(D)$ for the small (filled blue circles) and large (empty black circles) grains. The glued cobble flume bed is made out of small grains. The red dashed line shows the smart rock *b*-axis length of $D_{SR} = 0.09$ m. [Colour figure can be viewed at wileyonlinelibrary.com]

Table I. Expiremental flow conditions

Bed slope, S (grade)	Discharge, Q (l s^{-1})	Flow depth, H (m)	Flow velocity U_{avg} (m s^{-1})	Froude number, Fr	Number of smart rocks	Transport stage for smart rocks
0.02	159	0.14	1.09	0.93	0	−0.074
0.02	301	0.20	1.50	1.08	1	0.323
0.02	499	0.27	1.84	1.14	0	0.786
0.05	200	0.11	1.72	1.64	8	0.246
0.05	400	0.18	2.18	1.64	11	0.984
0.05	600	0.24	2.46	1.60	5	1.65
0.08	153	0.09	1.51	1.55	5	0.109
0.08	289	0.13	2.09	1.82	6	0.601
0.08	392	0.16	2.39	1.91	4	0.971
0.08	517	0.19	2.66	1.95	8	1.46

significant at steep slopes due to the use of a highly permeable cobble bed in our experiments (i.e. flow velocity is non-zero at the average-bed elevation). By predicting the depth-averaged stream-wise subsurface flow velocity U_{sub} using the approach of Lamb *et al.* (2017b) (see Equation 14 therein), we calculate the depth-averaged stream-wise flow velocity (excluding subsurface flow) U_{avg} as $U_{avg} = (Q - Q_{sub})/HW$, where Q is total flow discharge measured with an in-line magnetic flow meter, H is flow depth and $Q_{sub} = \eta W U_{sub}$ is the subsurface flow discharge, $W = 1$ m being channel width and $\eta = 28$ mm being the thickness of the subsurface layer. The surface flow has a nearly logarithmic vertical velocity profile far above the bed, while flow velocity decreases less than logarithmically as the bed is approached (Lamb *et al.*, 2017b). Reduced turbulence intensity was observed near the bed for shallower flows, i.e. flows with increasing relative roughness (Lamb *et al.*, 2008b). Flow conditions were fully turbulent (Reynolds numbers larger than 10^3) and all flows but one (experiment at 0.02 grade slope with the lowest discharge) were supercritical (i.e. with Froude numbers larger than 1). Steady and uniform flow conditions were attained by adjusting outlet gate heights to ensure spatial flow accelerations less than 5% averaged across the center 9 m of the flume (i.e. the test section) (Lamb *et al.*, 2017b). In such a case, bed shear stress can be approximated with limited bias as $\tau_b = \rho u_*^2$, where ρ is water density and $u_* = \sqrt{gHS}$ is bed shear velocity, S being bed slope (tangent of the bed-slope angle). Bed roughness Reynolds number $\mathrm{Re}_{k_s} = u_* k_s/\nu \approx 10^5$ (where ν is water kinematic viscosity and $k_s = 3D_{50}$ (Kamphuis, 1974)) is consistent with typical mountain streams.

We investigated 10 flow configurations with varying channel slope S (0.02, 0.05 and 0.08 grades) and flow discharge (153 l s^{-1} < Q < 600 l s^{-1}, Table I). At each flow configuration we conducted a series of bedload transport experiments by manually dropping mixed natural and smart rock assemblies upstream of the flume test section. Smart rocks have a spheroidal, but non-spherical, geometry similar to natural grains (Figure 2b), with an intermediate *b*-axis diameter of $D_{SR} = 0.09$ m (Figure 2c). For natural grains we used two different mixtures of well-sorted, fluvial gravels: a set of small grains equivalent to the flume bed grains with median grain size $D_{50}^S = 0.045$ m, and a set of larger grains with $D_{50}^L = 0.07$ m. Sets of small and large grains had size distributions with similar standard deviation σ obtained from best fitting the

log-'raised cosine' distribution $p_D^S(D)$ and $p_D^L(D)$ defined in Tsai *et al.* (2012) to each grain size distribution (Figure 2c). We found $\sigma = 0.12$ (dimensionless; see Tsai et al., 2012). Critical Shields stress $\tau^*_{c,\mathrm{SR}}$ for initial motion of smart rocks, where τ^* is defined as $\tau^* = \tau_b/((\rho_s - \rho)gD)$, was inferred by measuring the dry friction angle $\phi_{0,\mathrm{SR}}$ from tilt-table experiments over a rough bed of similar grain size to the flume bed sediment (following Prancevic et al., 2014), and applying the model of Lamb *et al.* (2008b) (see Appendix A). We found $\tau^*_{c,\mathrm{SR}} = 0.021$ for $S = 0.02$, $\tau^*_{c,\mathrm{SR}} = 0.0315$ for $S = 0.05$ and $\tau^*_{c,\mathrm{SR}} = 0.0451$ for $S = 0.08$. We extrapolated these findings to the other natural grains (NG) using a hiding function for gravel mixtures, $\tau^*_{c,\mathrm{NG}} = \tau^*_{c,\mathrm{SR}}(D_{\mathrm{NG}}/D_{\mathrm{SR}})^{-\alpha}$ with $\alpha = 0.9$ (Parker, 1990).

We performed the sediment transport experiments by sequentially dropping a given number N ($N = 1, 3, 10, 100, 370$ and 750) of natural cobbles mixed with a few (one to five) smart rocks into the test section. To investigate grain size dependency, we used sets of 370 small natural cobbles (with no smart rocks), chosen such that the total sediment mass was similar to that of the 100 larger cobbles. This procedure with instantaneously dropped grains allowed us to avoid the use of the sediment recirculation system, which generates seismic noise that overwhelms the bedload-induced noise. However, a drawback is that sediment flux q_b varies in time as the sediment pulse travels downstream. q_b gradually increased as grains progressively were entrained from where they were dropped, then reached a maximum and finally decreased as grains were deposited at the end of the test section. For all experiments with 1–370 cobbles there was a 1 s to several seconds time window during which all grains moved simultaneously; i.e. grains at the tail of the sediment pulse started to move before grains at the head reached the end of the test section. Since this time window corresponded to the time window of maximum seismic energy (see 'Seismic noise measurements', below), sediment flux during this time could be calculated a posteriori as $q_b = N\int_D \frac{p_D(D)V(D)u_S}{WL}$ (see Appendix B), $V(D) = 4\pi/3(D/2)^3$ being grain volume, L the spatial sediment pulse length and u_S the average sediment downstream velocity calculated from the difference between the first and the last impact recorded by smart rocks as they cover the flume test section. In these estimates, uncertainties on the prescribed sediment flux q_b are mainly due to uncertainties on the cobble-pulse length L, which, based on video analysis and direct observations, varied between 2 and 8 m. We use $L = 4$ m to calculate q_b and note that there is a factor of 2 uncertainty in q_b due to this consideration. In experiments with 750 cobbles, however, there was not a time window during which all grains were transported because the head of the sediment pulse reached the end of the test section before the tail started to move. In that case we calculated maximum sediment flux from video analysis (see Appendix B), which we then were able to relate to maximum seismic power.

Smart rock calibration, methods and experimental plan

Smart rock characteristics

A smart rock consists of an aluminium casing of typical river grain geometry that incorporates a three-component accelerometer measuring acceleration along three orthogonal axes (Figure 2b). Smart rocks have a density of $\rho_s = 2.6\ \mathrm{kg\,m^{-3}}$ made similar to that of natural rocks by incorporating thin lead plates into the aluminium of the smart rock. The embedded accelerometer has a sufficiently high sampling rate (512 Hz) and maximum acceleration range ($250g$, where $g = 9.81\ \mathrm{m\,s^{-2}}$ is acceleration due to gravity) to identify impacts and measure acceleration changes undergone by the smart rock under the typical (of the order of $1\ \mathrm{m\,s^{-1}}$) impact velocities investigated in our experiments (Appendix C).

Impact mechanics of smart rocks

We inferred underwater impact mechanical properties from evaluating the acceleration time series $a(t)$ recorded by smart rocks during multiple drop experiments conducted on top of the flume cobble bed and under still water (see Figure 3a). We measured impact times of the order of 3–6 ms, such that the acceleration time function expected during the impact had a nearly flat spectrum below 100 Hz, and the instantaneous impact assumption originally proposed by Tsai *et al.* (2012) was valid in our experiments (Appendix C). We measured the constant γ (Equation (4)) from time integrating the vertical acceleration time series, picking the incident (negative) velocity $w_{\mathrm{inc}}^{\mathrm{drop}}$ and the reflected (positive) velocity $w_{\mathrm{ref}}^{\mathrm{drop}}$ and averaging among all experiments, and calculating γ as $\gamma = 1 + |\bar{w}_{\mathrm{ref}}^{\mathrm{drop}}/\bar{w}_{\mathrm{inc}}^{\mathrm{drop}}|$. We found $\gamma = 1.13$, which corresponds to a coefficient of restitution $e = 0.13$, which is smaller than previously found in dedicated experiments (of the order of 0.6–0.9) for similar materials (steel and rocks) and regardless of whether impacts occurred in air or in more viscous fluids like water (Jackson *et al.*, 2010; Durda *et al.*, 2011). This discrepancy may be due to a geometrical effect relevant to bedload impacts, in which grains hit each other with their

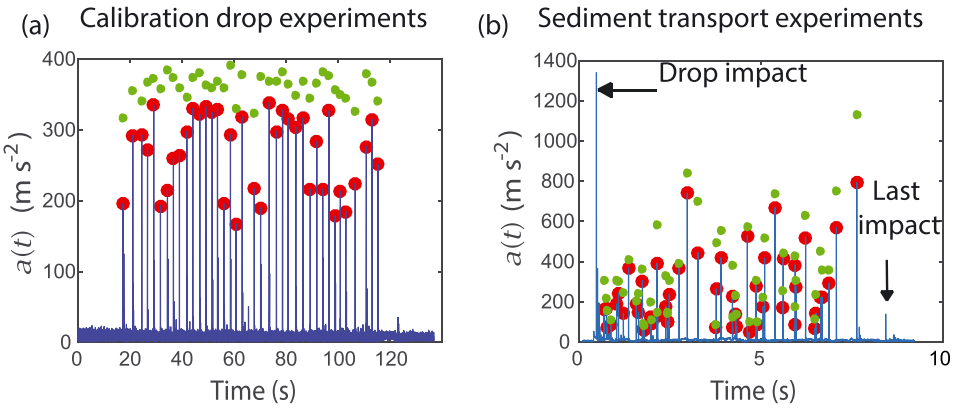

Figure 3. Examples of typical smart rock acceleration measurements acquired as a function of time for (a) calibration drops (4 cm height drops for 40 side-looking smart rock impacts) with horizontal bed and (b) a bedload transport experiment at 0.05 grade slope and 400 $\mathrm{l\,s^{-1}}$ discharge. Big red dots indicate acceleration maxima automatically picked for each impact. Small green dots indicate integrated acceleration values obtained by summing three acceleration measurements around each impact. [Colour figure can be viewed at wileyonlinelibrary.com]

center of mass not being perfectly aligned, such that extra impact energy loss occurs through grain rotation and deflection. It is also possible that this discrepancy is partly due to the specifics of our experimental setup, in which the impacted river bed grains are glued to a deformable epoxied fiberglass sheet, making the mechanical response of the ensemble particularly inelastic and thus γ particularly small. Thus, although our inferred γ is representative of our experiments, it might not be applicable to other experimental and natural settings.

Particle transport kinematics from smart rocks

In contrast to more common techniques (e.g. high-speed photographic techniques) that only allow particles with large motions to be measured over a restricted, pluridecimetric, subset of their trajectories (Nino *et al.*, 1994; Francis, 1973; Nino and Garcia, 1998; Abbott and Francis, 1977; Hu and Hui, 1996; Chatanantavet *et al.*, 2013), the use of smart rocks in this study allows us to quantify the full dynamics of bedload grain impacts along an entire grain trajectory, including potential periods of rest, sliding, rolling or saltation. We calculated impact hop times t_l as the time between impact-induced acceleration spikes, and the average downstream velocities of transported sediments u_s from the time between the first and last smart rock recorded impact and the corresponding 9 m distance along the flume test section (see Figure 3b). Inferring impact velocities during bedload experiments, however, cannot be done by integrating the entire acceleration time series, as done previously for drop experiments, because large and unresolvable rotations occurred between impacts. Thus we calculated v_l (see Figure 1b) as $v_l = \delta v/\gamma$, where δv is the velocity variation observed due to the impact (Appendix C) and $\gamma = 1.13$ is used based on the still-water calibration performed previously ('Impact mechanics of smart rocks', above). Doing this, we assume that impact energy loss under still water was similar to that under flowing water, which is supported by the fact that no change was observed in the average contact time, nor in the average of ratios between maximum absolute acceleration (see red dots in Figure 3a). We calculate absolute acceleration from integrating over the three measurement points from before and after the impact (see green dots in Figure 3b). We note that the impact velocity v_l measured from smart rocks corresponds to that oriented normal to the local bed topography, as opposed to w_{inc} used in Tsai *et al.* (2012) that corresponds to the vertical component of the incident impact velocity (Figure 1b). We also note that the smart rocks malfunctioned several times, which resulted in significant data gaps during certain experiments. The number of smart rock records is thus not constant from one experiment to another, and is particularly low for the 0.02 grade slope experiments since only one smart rock recorded useable data in those cases (see Table I). In the following sections, values of impact hop times, downstream velocities and impact velocities averaged along each smart rock trajectory and over all smart rock records of a given flow condition are denoted by $\bar{t}_l$, u_s and $\bar{v}_l$. Smart rock downstream velocities u_s are typically averaged over ~1 to 11 measurements. Given that one smart rock traveling the flume test section undergoes between about 35 (for 0.08 grade slope and $Q = 517\ \mathrm{l\,s^{-1}}$) and 110 (for 0.02 grade slope and $Q = 327\ \mathrm{l\,s^{-1}}$) impacts, average impact velocities $\bar{v}_l$ and hop times $\bar{t}_l$ are integrated over hundreds of measurements.

Seismic noise measurements and Green's function calibration

Seismic noise measurements

Seismic flume motion was recorded by a seismometer placed on the steel armature of the flume about halfway between the upstream and downstream ends of the test section (Figure 2a), which is connected to the steel floor of the flume. Vertical seismic power was calculated using vertical component seismograms and Welch's averaging method (Welch, 1967) applied on 1 s time windows with 50% overlap. Figure 4 shows examples of seismic power time series obtained during experiments at 0.08 grade slope with 100 large cobbles and

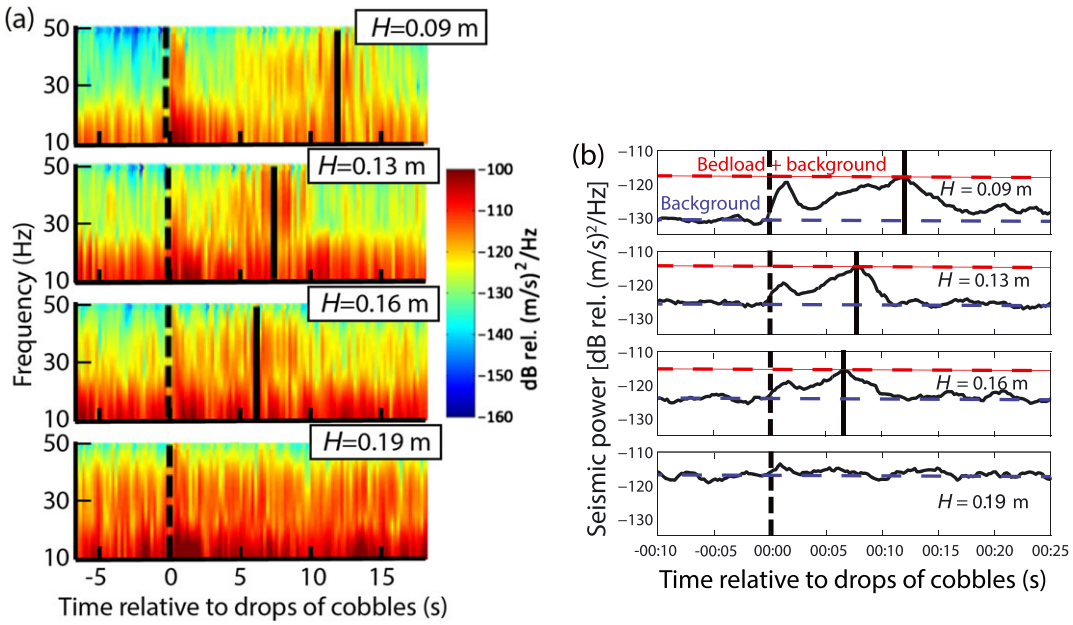

Figure 4. Examples of seismic power records during 0.08 grade slope experiments with 100 cobbles of the large grain set and under various flows depths (H) indicated. (a) Seismic power (see color scale) as a function of time and seismic frequency. (b) Seismic power averaged in the 25–50 Hz frequency range as a function of time (solid black line). Average values of background noise and bedload plus background noise are shown as the blue and red dashed lines, respectively. Vertical dashed lines in (a) and (b) indicate the time at which cobbles were dropped into the flume, and vertical solid lines correspond to the time at which seismic energy is maximal in the 25–50 Hz frequency range. [Colour figure can be viewed at wileyonlinelibrary.com]

various flow depths. Seismic noise due to grain impacts from bedload transport is thus mostly observed at relatively high frequencies and is best tracked in the 25–50 Hz frequency range, where a clear seismic power increase is often observed when bedload transport occurs (Figure 4b and Appendix D). Flume resonance is accounted for in model predictions through Green's function calibrations (see below). Bedload-induced noise is extracted from total noise by (i) picking the maximum seismic power value observed in the 25–50 Hz frequency band (see horizontal red dashed lines in Figure 4b), which corresponds to maximum sediment flux as quantified a posteriori (see 'Flume setup and flow/sediment transport conditions', above) and (ii) removing the background seismic noise contribution obtained by averaging the 25–50 Hz seismic power over identical conditions, but 1 min prior to the introduction of the sediment cobbles (see horizontal blue dashed lines in Figure 4b). This background noise is mainly due to noise from pumps and/or water pipe resonances, such that the turbulent flow induced-noise theory of Gimbert *et al.* (2014) cannot be tested from these experiments. In addition, for several cases the peak of seismic energy due to cobbles simultaneously moving as bedload was not visible because it was overwhelmed by noise from water pumps, which was particularly high at larger discharges (see, for example, the maximum flow depth experiment in Figure 4). We disregard these cases and only consider cases for which a clear seismic power maximum due to bedload could be distinguished by eye.

Green's function calibration

To predict seismic power in our experiments using Equations (1) and (2), we need to define the vertical-to-vertical flume Green's function $G_{F,2}(t)$. We measured $G_{F,2}(t)$ empirically by recording flume seismic motion due to the impact of a cobble of known mass $m = 0.66$ kg dropped from a known height $z^{\text{drop}} = 40$ cm on the flume bed with glued cobbles (Appendix D). We conducted this experiment on the tilted flume, such that flume seismic response could be probed in a geometrical situation similar to that of bedload experiments, and directly in air to avoid flowing water conditions. Using a reference measurement conducted at a given location (see black dot in Figure 5), we found an average amplitude of $\bar{G}_{F,2}(25 < f < 50) = 7.66 \times 10^{-8}$ m s^{-1}/N in the 25–50 Hz seismic frequency range of interest for bedload ('Seismic noise measurements', above). By applying such a measured Green's function to the bedload sediment transport experiments, we assume that flume seismic response is similar whether the flume is wet or dry. This assumption is supported by the fact that the flume's total mass is only marginally affected by the presence or absence of water, which represents at most one-fifth of the total flume mass, and that the water layer is too thin (at most 30 cm deep flows) for acoustic wave resonance in the water column to significantly enhance seismic power in the frequency range of interest.

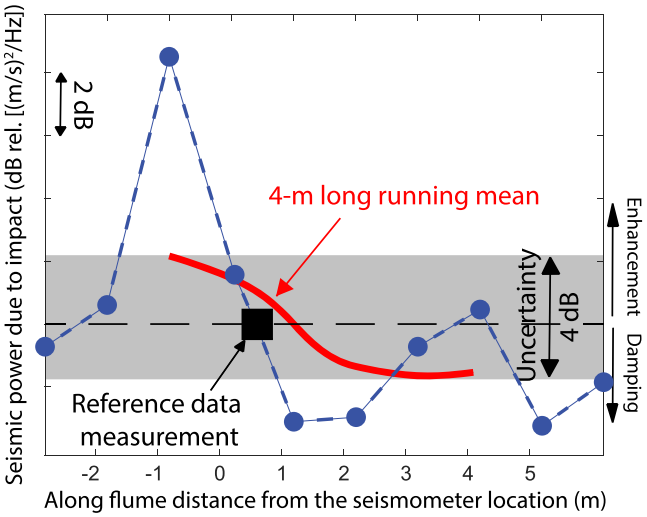

Figure 5. Measured along-channel variations of seismic velocity power (in the 25–50 Hz bedload frequency range) due to cobble impacts of uniform amplitude prescribed at various places along the flume test section. The black square corresponds to the reference impact point used to define the reference Green's function, and the blue dots correspond to other impact points. A 4 m long running mean (solid red line) of the linearly interpolated measurements (blue dashed line) is shown for uncertainty estimates in model predictions. [Colour figure can be viewed at wileyonlinelibrary.com]

We tested the spatial variation of the 25–50 Hz Green's function by evaluating the variations (amplification or damping) of observed seismic flume velocity power for similar impacts at various places along the flume test section (see blue dots in Figure 5). Seismic power was observed to vary by up to 10 dB in places, such that the spatial dependence of the bedload pulse during transport has to be accounted for in model predictions. We do so by approximating the sediment seismic source as being uniformly distributed (i.e. uniform bedload flux, impact velocities and rates) over a 4 m long bedload pulse traveling over the entire flume test section. We estimate the seismic response for such a 4 m long uniform seismic source by calculating the 4 m long running mean (see red line in Figure 5) of the seismic power spatial variations after linear interpolation between the individual measurements (see blue dashed line). We find that signal enhancement or damping along the flume test section for such a 4 m long uniform seismic source may cause bedload-induced seismic power to vary by ±2 dB around that predicted using the reference Green's function power $\bar{G}_{F,2}$ as defined previously from our reference point. This ±2 dB uncertainty in flume response is shown as error bars in the following model predictions. Although the bedload pulse may actually vary from 2 m to 9 m (i.e. the test section length) among experiments, these variations are expected to have negligible effect on our estimated uncertainty (see Figure 5).

Application of the modeling framework to the experiments

Using an average vertical-to-vertical flume Green's function $\bar{G}_{F,2}(f)$ as defined above, the predicted flume seismic power from the integral of all bedload sources (Equation (7)) simplifies to

$$P(f) = L \int_D \int_{t_l} p_l(t_l) \frac{n_D}{t_l} F_l^2(f, D, t_l) \bar{G}_{F,2}^2 \, \mathrm{d}t_l \, \mathrm{d}D \qquad (10)$$

For bedload experiments only made out of single-sized smart rocks, the size distribution of transported grains reduces to a delta function and the previous equation further simplifies to (using Equation (4) to rewrite the source term $F_l(f, D, t_l)$ with v_l instead of w_{inc}, and Equations (3) and (6) to substitute the function E_l)

$$P_{\text{SR}}(f) = \frac{N_{\text{SR}}}{\bar{t}_l} E_l(\tau_{\text{stage, SR}}) \, (\gamma \rho_s V_{\text{SR}} \bar{v}_l)^2 \, \bar{G}_{F,2}^2 \qquad (11)$$

where V_{SR} is the volume of each smart rock, v_l is the impact velocity oriented normal to the bed roughness (Figure 1b) as measured from the smart rocks ('Particle transport kinematics from smart rocks', above), and E_l is the impact efficiency

parameter that accounts for the role of impact velocity and rate distributions on seismic power, which we calculate as a function of transport stage $\tau_{\text{stage, SR}} = \tau^*/\tau^*_{c,\text{SR}} - 1$ (Equation (5)) as

$$E_I(\tau_{\text{stage, SR}}) = \frac{\int_{t_I} p_I(t_I) \frac{v_I(t_I)^2}{t_I(\tau_{\text{stage, SR}})} \mathrm{d}t_i}{\frac{\bar{v}_I^2}{\bar{t}_I(\tau_{\text{stage, SR}})}}. \tag{12}$$

We extend seismic power predictions to experiments with natural grains (NG) by defining their number per unit grain size as $n_D(D) = \frac{p_D(D) N_{\text{NG}}}{L}$ (see Appendix B), where N_{NG} is the number of natural grains. Then we assume that the function $E_I(\tau_{\text{stage, NG}})$ remains valid for all natural grains of various sizes and use Equation (10) to obtain

$$\begin{aligned} P_{\text{NG}}(f, \mathbf{x}) = N_{\text{NG}} \int_D \frac{p_D(D)}{\bar{t}_I(\tau_{\text{stage, NG}})} E_I(\tau_{\text{stage, NG}}) \\ \times (\gamma \rho_s V_{\text{NG}} \bar{v}_I(D))^2 \, \bar{G}^2_{F,2} \, \mathrm{d}D. \end{aligned} \tag{13}$$

Predictions of total seismic power for mixed smart rock and natural settings can thus be determined as

$$P(f, \mathbf{x}) = P_{\text{SR}}(f, \mathbf{x}) + P_{\text{NG}}(f, \mathbf{x}) \tag{14}$$

and the respective numbers of transported grains can be inverted as

$$\begin{aligned} N^{\text{inv}}_{\text{SR}} &= \xi P^{\text{obs}}(\mathbf{x}) \frac{\bar{t}_I(\tau_{\text{stage, SR}})}{E_I(\tau_{\text{stage, SR}}) \, (\gamma \rho_s V_{\text{SR}} \bar{v}_I(D_{\text{SR}}))^2 \, \bar{G}^2_{F,2}} \\ N^{\text{inv}}_{\text{NG}} &= (1-\xi) P^{\text{obs}}(\mathbf{x}) \frac{1}{\int_D \frac{E_I(\tau_{\text{stage, NG}})}{\bar{t}_I(\tau_{\text{stage, NG}})} p_D(D) \, (\gamma m \bar{v}_I(D))^2 \, \bar{G}^2_{F,2} \, \mathrm{d}D} \end{aligned} \tag{15}$$

where $\xi = N_{\text{SR}}/(N_{\text{NG}} + N_{\text{SR}})$ is the fraction of smart rock versus natural grain numbers and P^{obs} corresponds to observed seismic power. Inverted grain numbers can finally be converted into an inverted sediment flux q_b^{inv} as

$$q_b^{\text{inv}} = q^{\text{inv}}_{b,\text{SR}} + q^{\text{inv}}_{b,\text{NG}} = N^{\text{inv}}_{\text{SR}} \frac{u_S V_{\text{SR}}}{WL} + N^{\text{inv}}_{\text{NG}} \int_D \frac{p_D(D) V_{\text{NG}}(D) u_S}{WL} \, \mathrm{d}D. \tag{16}$$

Results

Particle transport kinematics

Particle kinematics for individual particles

We analyze particle transport kinematics for isolated moving particles by considering smart rock records for experiments with 1, 3 and 10 cobbles only. Figure 6 shows the measured average downstream bedload velocity u_S and incident impact velocity $\bar{v}_I$ for all flow configurations (see also Table I) as a function of transport stage $\tau_{\text{stage}} = \tau^*/\tau_c^* - 1$ (Figures 6a, 6b), and as a function of depth-averaged downstream flow velocity U_{avg} (Figures 6c, 6d), where the average excludes subsurface flow. u_S and $\bar{v}_I$ versus τ_{stage} in log-log space are linearly best fit by the power laws $u_S = 1.19\sqrt{R_g g D}\tau^{0.30}_{\text{stage}}$ ($R^2 = 0.64$) and $\bar{v}_I = 0.51\sqrt{R_g g D}\tau^{0.25}_{\text{stage}}$ ($R^2 = 0.53$) with g the acceleration due to gravity and $R_g = (\rho_s - \rho)/\rho$ the excess grain density, ρ_s being grain density. Empirical relations from Sklar and Dietrich (2004) (see discontinuous green lines in Figure 6a) roughly capture the general trend of u_S versus τ_{stage}, where u_S is either calculated as $u_S = 1.56\sqrt{R_g g D}(\tau^*/\tau_c^* - 1)^{0.56}$ (see dashed line) or as $u_S = 0.83\sqrt{R_g g D}(\tau^*/\tau_c^*)^{0.83}$ (see dotted line).

Although $\bar{v}_I$ as measured here corresponds to the impact velocity normal to the bed roughness and thus differs from the vertical component of impact incident velocity $\bar{w}_{\text{inc}}$ as defined in Tsai *et al.* (2012) (Figure 1), $\bar{v}_I$ can be well approximated by $\bar{w}_{\text{inc}}$ (Figure 6b) as predicted by Tsai *et al.* (2012), who used Lamb *et al.* (2008a) to calculate

$$\bar{w}_{\text{inc}}(H_b) = w_{\text{st}} \cos\theta \sqrt{1 - \exp[-\hat{H}_b]} \tag{17}$$

where H_b is the bedload layer height calibrated as

$$H_b = 1.44 D \left(\frac{\tau^*}{\tau_c^*}\right)^{0.50} \quad \text{for } H_b \leq H \text{ and } H_b = H \text{ otherwise} \tag{18}$$

from previous laboratory measurements (e.g., Nino *et al.*, 1994; Francis, 1973; Nino and Garcia, 1998; Abbott and Francis, 1977; Hu and Hui, 1996), w_{st} is the terminal settling velocity, defined as $w_{\text{st}} = \sqrt{4 R_g g D/(3 C_d)}$, $\hat{H}_b$ is the non-dimensional hop height defined as $\hat{H}_b = 3 C_d \rho H_b/(2 \rho_s D \cos\theta)$, $\theta = \arctan(S)$ is the bed slope angle and C_d is a drag coefficient that depends on particle Reynolds number and grain shape. Here we calculate C_d as in Tsai *et al.* (2012), using the empirical formula of Dietrich (1982) for a Corey shape factor of 0.8 and a Power roundness scale of 3.5 for natural gravel.

As expressed versus τ_{stage}, however, both u_S and $\bar{v}_I$ exhibit significant scatter. This scatter is mainly caused by an extra dependency of u_S and $\bar{v}_I$ on bed slope S. Expressing velocities as a function of slope after correcting for their τ_{stage}-dependency, i.e. expressing $u_S/1.19\sqrt{R_g g D}\tau^{0.30}_{\text{stage}}$ and $\bar{v}_I/0.51\sqrt{R_g g D}\tau^{0.25}_{\text{stage}}$ as a function of S, we find (Figures 6e, 6f)

$$u_S = (9.0S + 0.47) \times 1.19\sqrt{R_g g D}\tau^{0.30}_{\text{stage}} \tag{19}$$

and

$$\bar{v}_I = (10.4S + 0.4) \times 0.51\sqrt{R_g g D}\tau^{0.25}_{\text{stage}} \tag{20}$$

Scatter is reduced, R^2 values are improved and slope dependency is no longer significant when u_S and $\bar{v}_I$ are compared to average flow velocity U_{avg} instead of to transport stage τ_{stage} (Figure 6b). Reduced scatter was previously shown by Chatanantavet *et al.* (2013) for u_S, but was not reported for $\bar{v}_I$. Chatanantavet *et al.* (2013) originally proposed the empirical relationship $u_S = 0.6 U_{\text{avg}}$ based on best-fit data from a large catalogue including data originally compiled by Sklar and Dietrich (2004) and data representing hydraulically smooth beds. Best fits of our experiments with rough bed conditions gives $u_S = 0.91 U_{\text{avg}} - 0.50\sqrt{R_g g D}$ ($R^2 = 0.92$), which leads to similar values to $u_S = 0.6 U_{\text{avg}}$ in the range of Shields stresses investigated here, but is consistent with there being a threshold for motion. This threshold behavior for motion is consistent with our non-zero grain-to-bed friction boundary condition due to the rough bed, and the y-intercept likely depends on the critical Shields number for initial motion. To explain both our data and those analyzed in Chatanantavet *et al.* (2013), we propose that u_S may be described as

$$\begin{aligned} u_S = 0.6 U_{\text{avg}} \exp(-(U_{\text{avg},c}/U_{\text{avg}})^X) \\ \text{for } U_{\text{avg}} \geq U_{\text{avg},c} \text{ and } u_S = 0 \text{ otherwise} \end{aligned} \tag{21}$$

where $U_{\text{avg},c}$ is the depth-averaged velocity of the surface flow at the threshold for grain motion and X is a constant. An example of such scaling is shown in Figure 6c using $U_{\text{avg},c} = 1.4$ m s^{-1} and $X = 20$, although $U_{avg,c}$ likely depends on particle weight.

We also find that the measured average incident impact velocities $\bar{v}_I$ are linearly related to the measured depth-averaged surface flow velocities (Figure 6d), and thus to the average downstream bedload velocities u_S (Figure 7a).

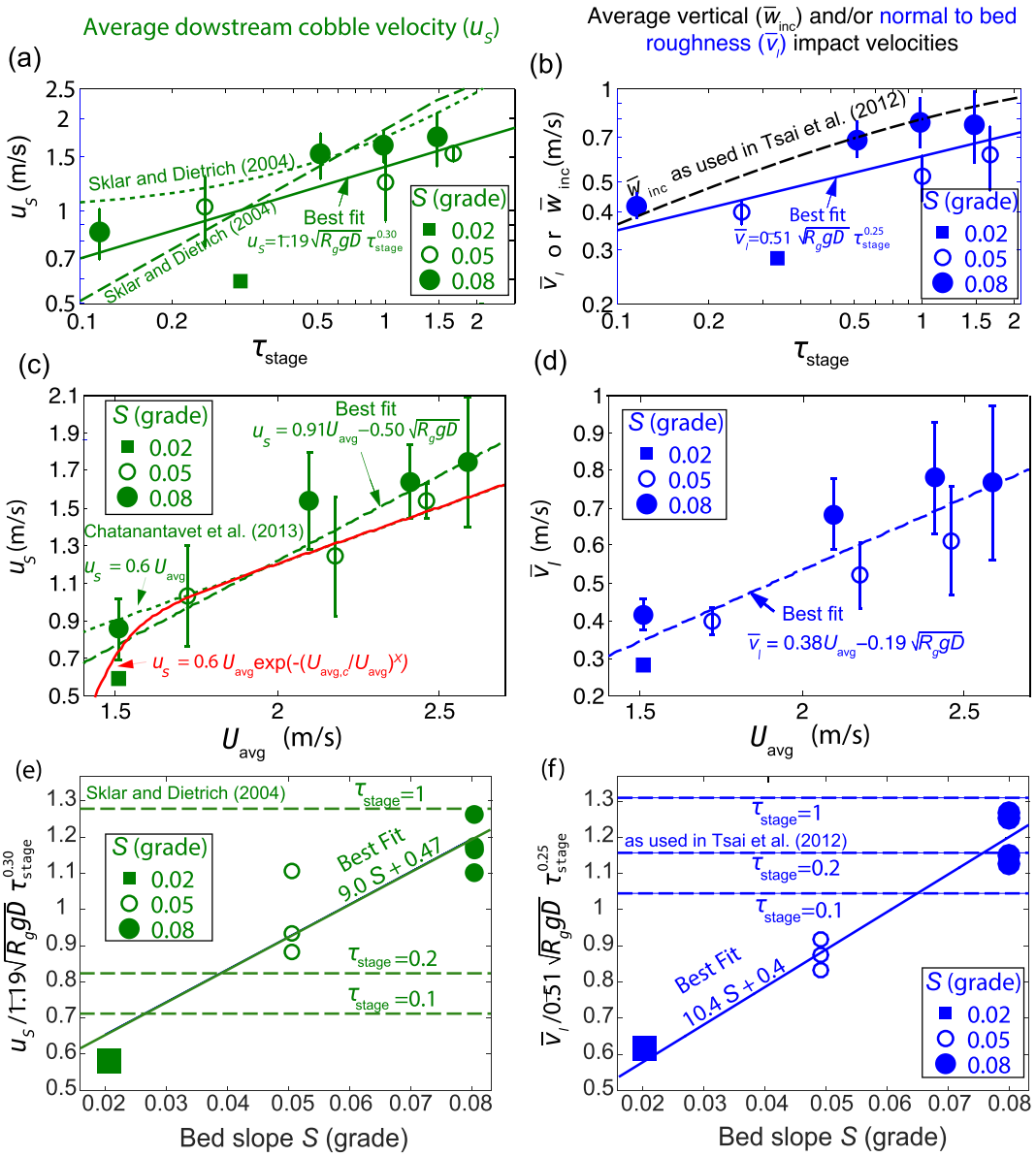

Figure 6. Average downstream cobble velocity u_S (green, left) and vertical and normal to bed roughness average velocities (right), $\bar{w}_{\text{inc}}$ (black) and $\bar{v}_l$ (blue), respectively, for the various flow configurations (see Table I) and as a function of (a, b) transport stage $\tau_{\text{stage}} = \tau^*/\tau_c^* - 1$, (c, d) depth-averaged flow velocity U_{avg} and (e, f) bed slope S once corrected from their τ_{stage}-dependency as $u_S/1.19\sqrt{R_ggD}\tau_{\text{stage}}^{0.30}$ and $\bar{v}_l/0.51\sqrt{R_gD}\tau_{\text{stage}}^{0.25}$. Using data from experiments with less than or equal to 10 cobbles. Symbols correspond to measurements, solid lines to best fits of our data and discontinuous lines to predictions from previously proposed empirical fits: using Sklar and Dietrich (2004) for u_S versus τ_{stage} (dashed line in a) and versus τ^*/τ_c^* (dotted line in a), Tsai *et al.* (2012) for $\bar{w}_{\text{inc}}$ versus τ_{stage} (dashed line in b, see Equation (17)) and Chatanantavet *et al.* (2013) for $u_s = 0.6U_{\text{avg}}$ (dashed line in c). Measurement error bars correspond to the standard deviation of the respective quantities calculated across smart rock records. The thin red line in (c) corresponds to a scaling of the type $u_S = 0.6U\exp(-(U_{\text{avg},c}/U_{\text{avg}})^X)$ for $U_{\text{avg}} \geq U_{\text{avg},c}$ and $u_S = 0$ otherwise, using $U_{\text{avg},c} = 1.4\ \text{m s}^{-1}$ and $X = 20$. Note that axes are logarithmic in (a, b) and linear in (c)–(f). [Colour figure can be viewed at wileyonlinelibrary.com]

All measurements follow a linear scaling of $\bar{v}_l = 0.43u_S$ ($R^2 = 0.94$) regardless of flow conditions.

The average time $\bar{t}_l$ between each impact as observed as a function of τ_{stage} in our experiments (see Figure 7b) scales similarly to that predicted in Tsai *et al.* (2012) using Sklar and Dietrich (2004) as

$$\bar{t}_l = H_b/(C_1 w_s) \tag{22}$$

with H_b calculated from Equation (18), $C_1 \approx 2/3$, which is a coefficient that accounts for the particle ejection or rise time being about 1.5 times larger than the fall time, and w_s the bedload average settling velocity defined as (Tsai *et al.*, 2012)

$$w_s = \frac{H_b}{\int_0^{H_b} w_l(z)^{-1}\,\mathrm{d}z} = \frac{\hat{H}_b w_{\text{st}}\cos\theta}{2\log\left[e^{\hat{H}_b/2} + \sqrt{e^{\hat{H}_b} - 1}\right]}. \tag{23}$$

However, while scaling is similar, the amplitude is about 2.5 times smaller (see Figure 7); i.e. impact rates $1/\bar{t}_l$ are about 2.5 times larger than those predicted by Sklar and Dietrich (2004). Predictions of $\bar{t}_l$ from Sklar and Dietrich (2004) can be approximated with $\bar{t}_l = 0.35(\tau^*/\tau_c^* - 1)^{0.28}$, while best fit of our data gives $\bar{t}_l = 0.14(\tau^*/\tau_c^* - 1)^{0.28}$ ($R^2 = 0.83$). Also, for a given value of τ_{stage}, there exists an extra dependency of impact times on slope, with impact times being shorter, i.e. impact rate being larger, with decreasing slope. This can explain why u_S and $\bar{v}_l$ exhibit an extra dependency (increase) with slope at constant τ_{stage} (Figures 6e, 6f), since more impacts at smaller slopes would reduce the average downstream velocity u_S and impact velocities $\bar{v}_l$.

Finally, we estimate the average impact velocity vector angle Θ_l relative to vertical (Figure 1b) from our independent

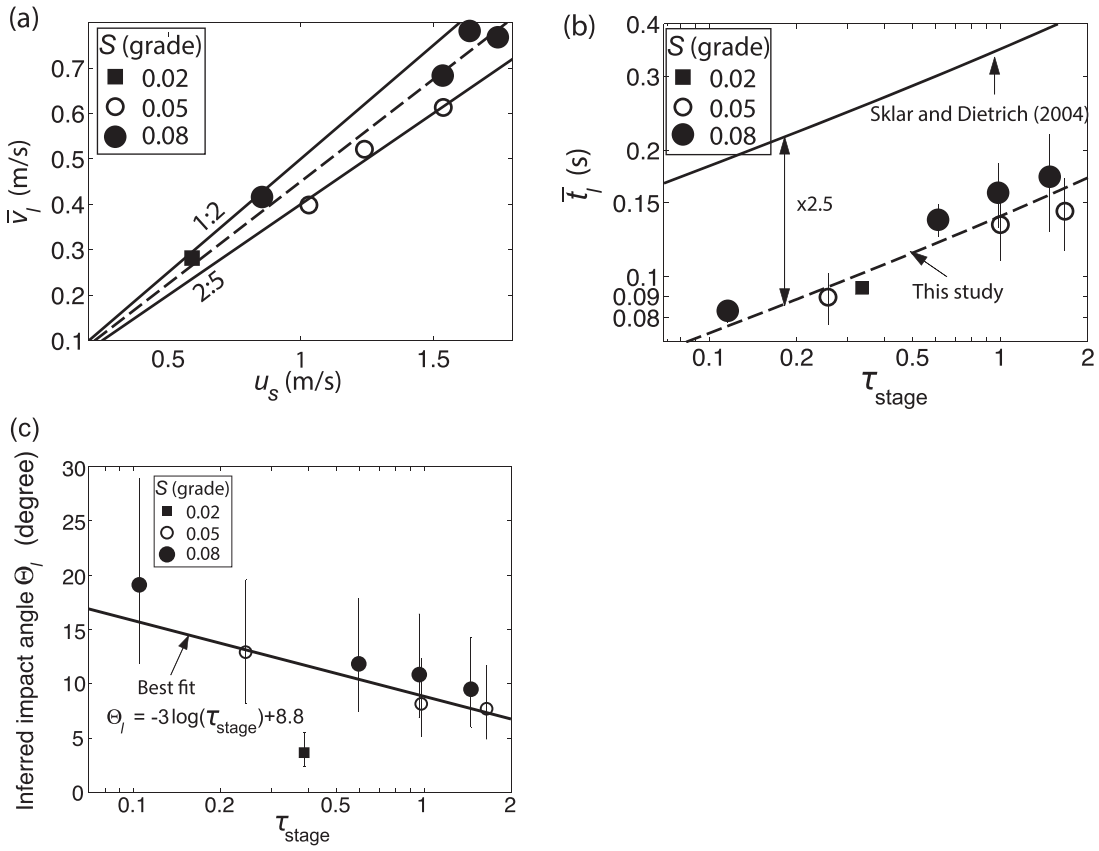

Figure 7. Impact properties and their links with fluvial parameters. Using data from experiments with less than or equal to 10 cobbles. (a) Observed average impact velocity $\bar{v}_I$ as a function of observed average downstream cobble velocity u_S. The dashed line shows best data fit ($\bar{v}_I = 0.43u_S$), and the solid lines show $\bar{v}_I = \frac{2}{5}u_S$ and $\bar{v}_I = \frac{1}{2}u_S$. (b) Average time $\bar{t}_I$ between impacts as a function of transport stage $\tau_{stage} = \tau^*/\tau_c^* - 1$. Error bars correspond to the standard deviation of average hop time calculated across smart rock records. The solid line shows predictions using $\bar{t}_I = H_b/(C_1 w_s)$, where H_b and w_s are calculated from empirical relationships by Sklar and Dietrich (2004; see Equations 18 and (23)). The dashed line shows $\bar{t}_i = 0.14\tau_{stage}^{0.28}$ that corresponds to the best fit to the data. (c) Impact angle Θ_I relative to vertical (see Figure 1b) as a function of τ_{stage}. Θ_I is calculated from our direct measurements of $\bar{v}_I$ and from estimates of v_{inc} (using plausible bounds for $\bar{u}_{inc}$ as a function of u_S and using Equation (17) to calculate $\bar{w}_{inc}$; see main text).

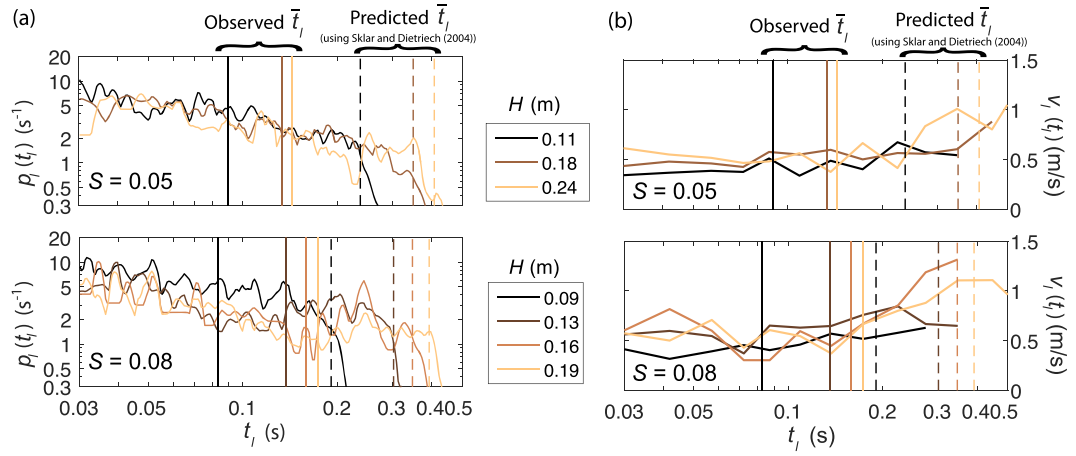

Figure 8. (a) Probability density distributions $p_I(t_I)$ (per unit time) of hop times and associated (b) impact velocities v_I as a function of hop time for (top) 0.05 grade slope and (bottom) 0.08 grade slope configurations. Vertical dashed lines show hop times predicted by Sklar and Dietrich (2004, using Equation (22)), while vertical solid lines show average values calculated from the distribution as $\bar{t}_I = \int_{t_I} p_I(t_I) t_I dt_I$. Using data from experiments with less than or equal to 10 cobbles. [Colour figure can be viewed at wileyonlinelibrary.com]

measurements of $\bar{v}_I$, u_S and $\bar{t}_I$. We use $\Theta_I = \pi/2 - (\Theta_{inc} + \Theta_{mod})$, where $\Theta_{inc} = \arctan(u_{inc}/w_{inc})$ is the impact incident angle with respect to horizontal, $\Theta_{mod} = \arccos(v_I/v_{inc})$ is the modified impact angle, and $v_{inc} = \sqrt{u_{inc}^2 + w_{inc}^2}$ is the norm of the incident velocity vector. We calculate the average impact angle Θ_I by first observing that the average downstream component $\bar{u}_{inc}$ of the impact velocity is directly proportional to u_S, and second calculating the vertical impact velocity $\bar{w}_{inc}$ using Equation (17) by substituting our observation that average hop time and thus hop height is 2.5 times smaller than that predicted using Equation (18). Marker values in Figure 7c are obtained using $\bar{u}_{inc} = u_S$, while error bars are obtained

by using $\bar{u}_{inc} = 2u_S$ (upper bound) and $\bar{u}_{inc} = 0.5u_S$ (lower bound). We find that the average impact angle Θ_I is small, about 5–20° from vertical, such that the force of impact is oriented nearly vertically (see Figure 1b). Since $\Theta_I = -\theta$ for a perfectly smooth bed, we conclude that the rough bed conditions only moderately affect the impact velocity vector angle. We finally note that Θ_I decreases (so that impacts are closer to perpendicular to the bed) when transport stage increases, consistent with grain trajectories being less perturbed by the bed roughness at larger transport stages.

Further insights into the dynamics of bedload can be gained from the analysis of the full statistical properties of impacts. For each flow configuration except that at 0.02 grade slope for which data sparsity does not allow representative statistics (only one smart rock record; see Table I), we calculate the probability density function $p_I(t_I)$ of hop times t_I as $p_I(t_I) = \frac{n_I(t_I)}{N_I\,dt_I}$ such that $\int_{t_I=0}^{\infty} p_I(t_I)\,dt_I = 1$ where $n_I(t_I)$ is the number of impacts occurring during the time interval $[t_I - dt_I/2, t_I + dt_I/2]$ and N_I is the total number of impacts recorded at a given flow condition (Figure 8a). Hop times are observed to be widely distributed with $p_I(t_I)$ remaining large down to 0.03 s, meaning that numerous impacts occur at hop times an order of magnitude smaller than those expected from bedload saltating grain predictions (Sklar and Dietrich, 2004; using Equation (22); see dashed vertical lines in Figure 8a as compared to solid vertical lines). The corresponding impact velocities $v_I(t_I)$ for these small hop times (Figure 8b) only weakly depend on flow conditions, and are distributed uniformly versus t_I for $t_I < 0.1$ s. In contrast, v_I significantly increases (by about a factor of two) and depends more strongly on flow conditions for $t_I > 0.1$ s. We do not expect these short hop times to be due to rolling or sliding because rolling and sliding are not expected at the high transport stages of these experiments. Instead, we interpret these short hop times as implying that sometimes multiple impacts with the bed occur at the end of a single saltation

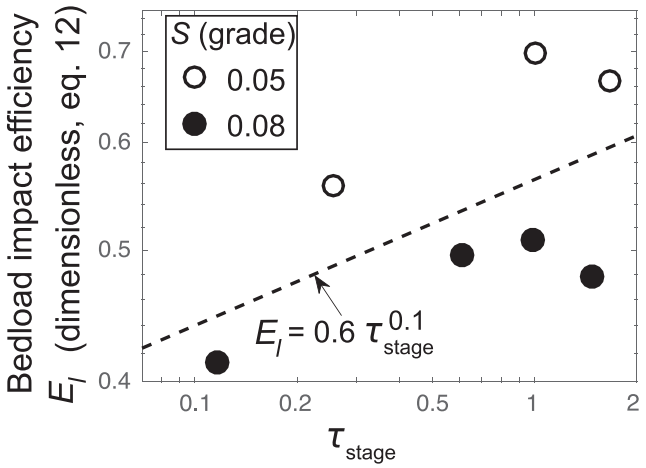

Figure 9. Values of the impact efficiency parameter E_I, which represents the control of bedload impact rate and velocity statistics on seismic noise power (Equation (12)), based on the full distributions of bedload hop times and impact velocities measured for the various flow conditions and as a function of transport stage (Figure 8). The dashed line corresponds to best linear fit in the log-log space, which is applied in Figure 12(a) to set E_i.

Table II. Summary of observed seismic power P^{obs} (dB) averaged in the bedload frequency range (25–50 Hz) as well as prescribed sediment flux q_b ($m^2\ s^{-1}$) for all conducted flume experiments with various slopes S, water discharge Q and dropped cobble numbers N

Exp. #	S (*grade*)	Q ($l\ s^{-1}$)	N	P^{obs} (dB)	q_b ($m^2\ s^{-1}$)
1	0.02	301	10	−129	4.2e−4
2	0.05	200	3	−133.1	3.2e−4
3	0.05	200	10	−129.3	7.4e−4
4	0.05	200	100	−123.5	4.3e−3
5	0.05	400	3	−131.3	3.8e−4
6	0.05	400	10	−126.6	8.9e−4
7	0.05	400	100	−122	5.2e−3
8	0.05	600	750	−113.6	5.5e−3
9	0.08	153	3	−130.5	2.6e−4
10	0.08	153	10	−125.3	6.1e−4
11	0.08	153	100	−118.3	3.6e−3
12	0.08	153	370 small	−129.4	3.6e−3
13	0.08	289	3	−128.9	4.7e−4
14	0.08	289	10	−124.8	1.1e−3
15	0.08	289	100	−114.6	6.4e−3
16	0.08	289	370 small	−126.9	6.4e−3
17	0.08	289	750	−118.5	1.1e−2
18	0.08	392	3	−125.6	5.0e−4
19	0.08	392	10	−121.2	1.2e−3
20	0.08	392	100	−115.9	6.9e−3
21	0.08	392	370 small	−122.7	6.9e−3
22	0.08	392	750	−115.1	1.1e−2
23	0.08	517	750	−114.4	1.55e−2

Note. Experiments with cobble numbers annotated 'small' are those conducted using the set of small grains (Figure 2c).

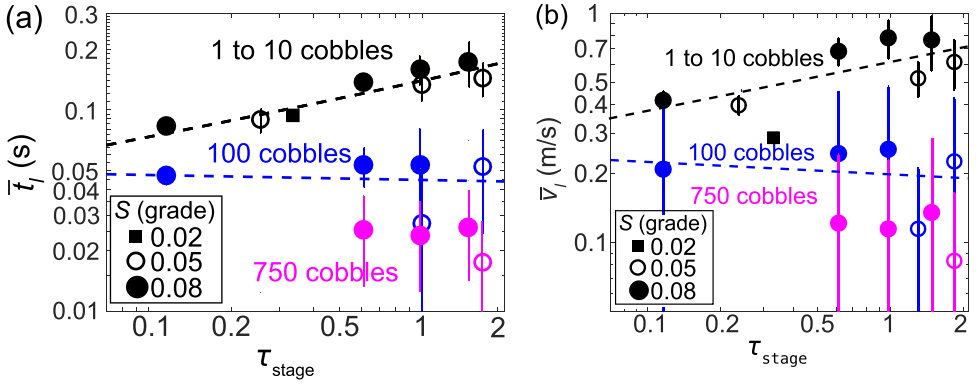

Figure 10. Average (a) time between impacts and (b) impact velocities as a function of transport stage for the 1 to 10 (black), 100 (blue) and 750 (magenta) cobbles experiments. Error bars correspond to the standard deviation of the respective quantities calculated across smart rock records. Dashed lines show the best linear fits $\bar{t}_i = 0.14\tau_{stage}^{0.28}$ and $\bar{v}_i = 0.51\sqrt{R_g g D}\tau_{stage}^{0.25}$ for tests with 1 to 10 cobbles, and $\bar{t}_i = 0.044\tau_{stage}^{-0.03}$ and $\bar{v}_i = 0.16\sqrt{R_g g D}\tau_{stage}^{-0.06}$ for tests with 100 cobbles. No meaningful fit could be done for tests with 750 cobbles due to lacking observations at low transport stage. [Colour figure can be viewed at wileyonlinelibrary.com]

hop. Multiple bed impacts might result from the saltating grain ricocheting off of neighboring particles on the bed before being ejected into the flow to begin the next saltation hop.

The impact efficiency parameter E_I, which represents the control of bedload impact rate and velocity statistics on seismic noise power (Equation (12)), is calculated from the smart rock records and shown as a function of τ_{stage} and for the various channel slopes in Figure 9. Measured values of E_I are significantly smaller than 1 ($E_I \approx 0.5$ is an appropriate approximation), and E_I is observed to increase with τ_{stage}.

Particle kinematics with many moving particles

Average times between impacts and impact velocities are shown for the 1 to 10, 100 and 750 cobble experiments as a function of transport stage in Figure 10. Experiments with 100–750 cobbles have average times between impacts and impact velocities about two to ten times smaller than those with fewer cobbles; i.e. grains undergo many (up to ten times) more impacts with much smaller (up to ten times) intensity as transport rate increases. Not only are absolute values of $\bar{t}_I$ and $\bar{v}_I$ modified at higher transport rates, but the scaling relations of $\bar{t}_I$ and $\bar{v}_I$ with respect to transport stage are also different. The significant increase of time between impacts and impact velocities observed with transport stage at low sediment flux (1–10 cobbles) is no longer observed for the higher transport fluxes of 100 and 750 cobbles, where $\bar{t}_I$ and $\bar{v}_I$ are nearly constant with transport stage, presumably due to the increased role of particle–particle collisions relative to particle-bed collisions.

Bedload-induced seismic noise and comparison to theory

Observations

Observed seismic power values P^{obs} averaged in the 25–50 Hz bedload frequency range (see 'Seismic noise measurements and Green's function calibration', above) are summarized in Table II for all experiments. All measured values of seismic power are shown as a function of prescribed bedload flux in Figure 11a. Although seismic power depends significantly on sediment flux, large scatter (deviations of up to 15 dB) is observed, as expected, due to a dependence on other parameters related to flow hydraulics and bedload transport characteristics.

Dependency of seismic power on model parameters

We evaluate the control of flow and sediment transport parameters on seismic power by examining subsets of the data and varying only one parameter across experiments. For experiments with varying sediment flux at a given slope (0.08 grade), a single water discharge (289 l/s) and thus flow depth (0.13 m) and a given set of grain sizes (using the large grain set), seismic power follows a linear scaling with sediment flux, as expected from Tsai *et al.* (2012) (see Figure 11b) and our revisited model. Experiments at high sediment flux are slightly off that scaling, although the limited number of observations prevents us from concluding whether the discrepancy is significant of not.

For experiments with varying water discharge and thus flow depth at a given slope (0.08 grade), a given set of grain sizes (using the large grain set) and constant (normalized by) sediment sediment flux, we observe no clear dependency of seismic power on flow depth or equivalently transport stage (Figure 11c). Given the sparsity and scatter of our data, this observation is consistent with both the predictions of Tsai *et al.* (2012) and the revisited model, although the revisited model predicts seismic power to weakly increase with flow depth, while it is predicted to decrease by Tsai *et al.* (2012). The predicted increase is due to the numerous impacts with short hop times (Figure 8a) and constant velocities (Figure 8b) regardless of transport stage observed in our experiments, and which are not accounted for in Tsai *et al.* (2012).

For experiments with varying grain diameter (from the small to the large grain set) at a given slope (0.08 grade), constant (normalized by) sediment flux, and for distinct values of water discharge (either 153, 289 or 392 l s^{-1}) and thus flow depth (0.09, 0.13 or 0.16 m), we observe a 10 dB increase in seismic power for an increase in grain diameter by a factor of 7/4.5 (see Figure 11d). This increase is mainly explained by the $P \sim D^3$-scaling predicted by Tsai *et al.* (2012), although this scaling underestimates the observed increase by about 2–4 dB. We do not yet have any explanation for this discrepancy, i.e. whether it is due to specifics of our experiments or to missing physics in the model.

Finally, for experiments with varying channel slope (0.05 and 0.08 grades) at constant transport stage $\tau_{stage} = 1$, and similar grain sizes (using the large grain set), we observe that seismic power, when normalized by sediment flux, strongly depends on slope since experiments at 0.08 grade slope generate about 4 dB more seismic power than experiments at 0.05 grade slope (see Figure 11e). This feature is not predicted by the model of Tsai *et al.* (2012) since impact velocities and rates therein only depend on slope indirectly due to the dependence on transport stage (Figure 6a). However, this finding is consistent with our smart rock observations that impact velocities have a dependency on channel slope in addition to that due to Shields stress (Figure 6f). Accounting for this impact velocity dependency in our improved model framework, we explain the full range of seismic power change with slope.

Observed versus predicted absolute seismic power using measured grain kinematics

We test predictions of absolute seismic power by holding sediment size and the number of grains constant using exclusively experiments with three smart rocks. Figure 12 shows predicted versus observed seismic power with and without accounting for bedload statistics, i.e. using either $E_I(\tau_{stage}) \approx 0.6\tau_{stage}^{0.1}$ or $E_I = 1$ in Equation (11). No model tuning has been done to match observed amplitudes since all model parameters were independently constrained previously from smart rocks and other dedicated measurements (see 'Experimental Strategy, Methods and Measurements', above). Predictions that account for bedload statistics are within ~3 dB of the observations, whereas predictions done without accounting for full bedload statistics (as in Tsai et al., 2012) lead to a slight, ~3 dB overestimate of observed seismic power.

We also use the entire dataset to evaluate the reliability of model predictions with varying grain size and number (see Table II and Figure 13a). We conduct model predictions for all experiments by neglecting grain–grain interactions at high sediment flux rates, i.e. assuming that grain kinematics as inferred with individual particles remain true for sets with many particles (100–750 grains). In addition, we assume the $\bar{t}_I$ versus τ_{stage} relationship (Figure 7b), and that the impact velocities $\bar{v}_I$ and downstream velocities u_S are independent of grain size (except through the Shields stress dependency) such that the $\bar{t}_I$ versus τ_{stage} relationship as well as values of $\bar{v}_I$ and u_S as inferred from smart rocks can directly be used for all other grains. This assumption for $\bar{v}_I$ and u_S is supported by both variables being observed to directly scale with depth-averaged flow velocity U_{avg} regardless of τ_{stage} (Figure 6d), while $\bar{v}_I$ and u_S as expressed as a function of τ_{stage}, i.e. as corrected for grain size relative to flow conditions, are more scattered

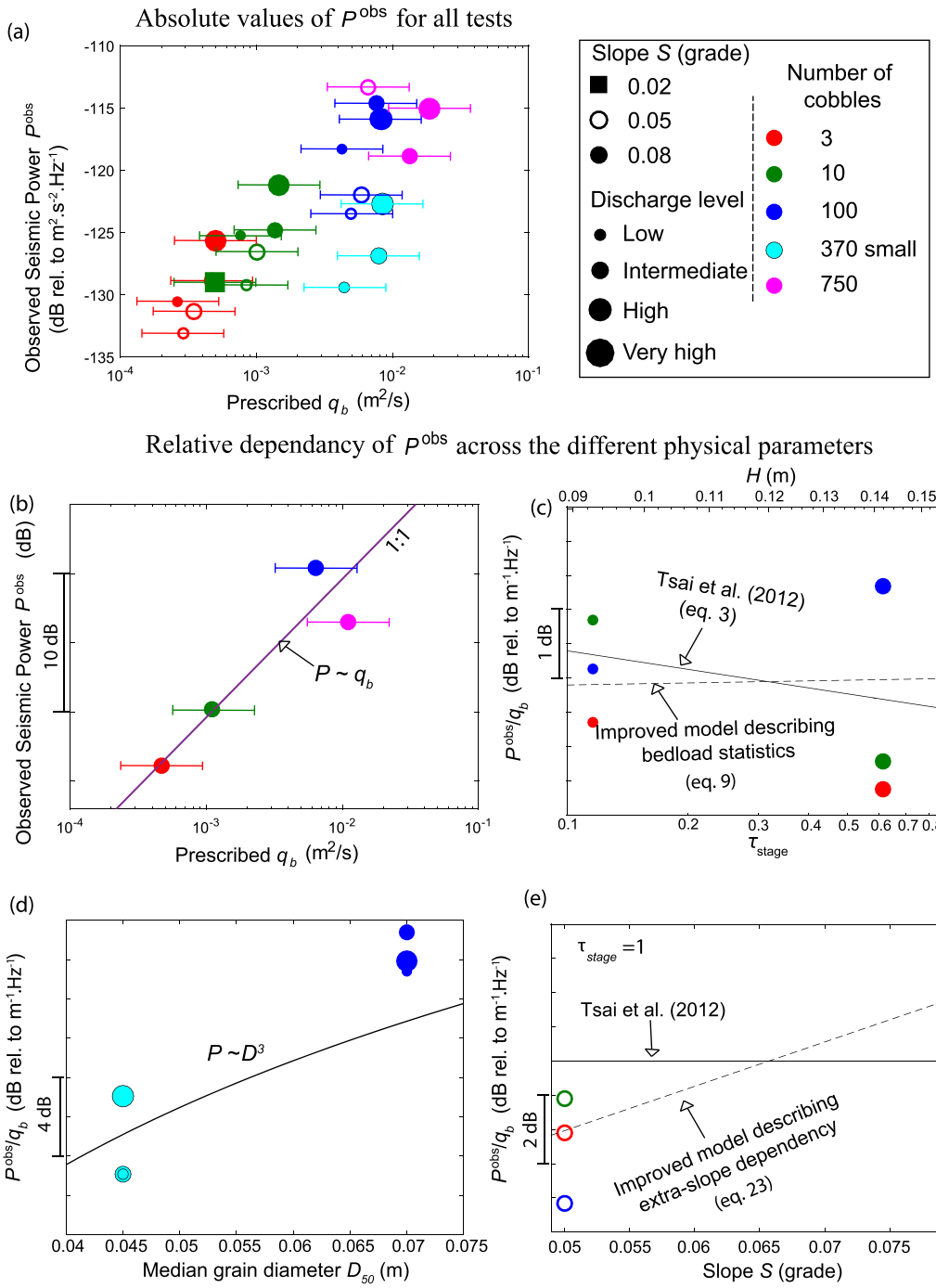

Figure 11. Measured bedload-induced, 25–50 Hz frequency seismic power P^{obs} (a) for all experiments as a function of sediment flux (see legend for symbol chart and corresponding experiment characteristics in Table II) and (b, c, d, e) for subsets of the data. (b) P^{obs} versus q_b for experiments at constant slope (0.08 grade) and discharge (289 l s^{-1}). The solid line shows the 1:1 scaling prediction. (c) Flux normalized seismic power P^{obs}/q_b versus τ_{stage} and/or H at constant slope (0.08 grade). The solid line shows the scaling prediction from Tsai *et al.* (2012) and the dashed line shows that of our improved model. (d) Flux normalized seismic power P^{obs}/q_b versus D_{50} for 0.08 grade slope experiments at multiple discharges (153, 289 or 392 l s^{-1}). The solid line shows the $P \sim D^3$ model prediction. (e) Flux normalized seismic power P^{obs}/q_b versus channel slope S at τ_{stage}=1. The solid line shows the scaling prediction from Tsai *et al.* (2012) and the dashed line shows that of our improved model. [Colour figure can be viewed at wileyonlinelibrary.com]

(Figure 6b). Based on a similar argument, we also assume that the impact efficiency parameter $E_I(\tau_{stage})$ as empirically defined previously holds across all grain sizes.

Predictions versus observations of seismic power collapse onto a nearly one-to-one line (within 3 dB accuracy) for most experiments (Figure 13a). These accurate predictions translate into accurate inversions of sediment flux from seismic noise, with inverted values of sediment fluxes falling within a factor of two uncertainty from prescribed ones (Figure 13b) over nearly two orders of magnitude. Estimating sediment flux at transport capacity using the empirical relationship of Fernandez-Luque and van Beek (1976) as $q_{bc} = 5.7\sqrt{R_g g D_{50}^3}(\tau^*(D_{50}) - \tau_c^*(D_{50}))^{3/2}$ (where D_{50} is the median grain size of the considered set of moving grains), we find that the sediment fluxes investigated here are more than an order of magnitude lower than those expected at transport capacity. We note, however, that our estimates of q_{bc}, and thus the ratio q_b/q_{bc}, should be taken with caution because q_{bc} is asso-

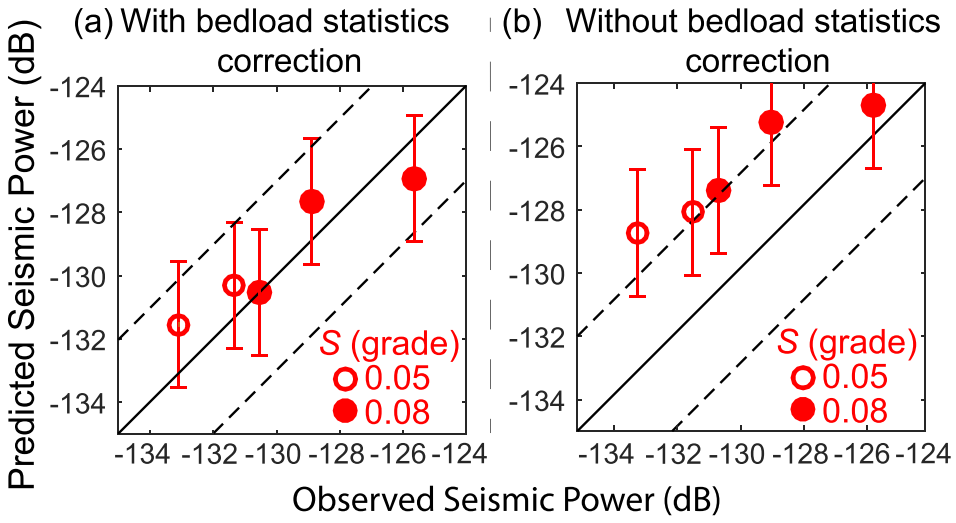

Figure 12. Predicted versus observed high-frequency (25–50 Hz) seismic power for all experiments with three smart rocks. Model predictions use Equation (11), in which the impact efficiency parameter E_I is set to (a) $E_I = 0.6(\tau^*/\tau_c - 1)^{0.1}$ (accounting for bedload statistics) and to (b) $E_I = 1$ (not accounting for bedload statistics). Symbols indicate slope (see legend). All other parameters used in model predictions ($\bar{v}_I$, u_S and $\bar{t}_I$) are directly set from the smart rock measurements. [Colour figure can be viewed at wileyonlinelibrary.com]

ciated with significant (at least a factor of two) uncertainty, and may be overestimated here (q_b/q_{bc} underestimated) due to our experiments not allowing interchange of transported grains with those of the bed (contrary to those of Fernandez-Luque and van Beek, 1976), in which case D_{50} would be smaller. Nevertheless, despite significant particle–particle interactions (i.e. impacts) occurring between transported grains at the highest fluxes (see Figure 10), we find that our model based on the description of particles moving individually, and thus solely interacting with the bed, still yields appropriate predictions. This could be explained by particle-bed impacts at the highest fluxes (with significant particle–particle impacts) being less energetic but more frequent than expected for individually moving particles at lower fluxes, such that the two effects largely cancel out and use of formulas based on individually moving particles still yield appropriate predictions at the highest fluxes.

Observed versus predicted seismic power using empirical relationships for grain kinematics

Here we investigate how much uncertainty is added to model predictions when using empirical estimates instead of the smart-rock measured quantities as used in the previous subsection. Figures 13c and 13d show inverted normalized sediment transport fluxes q_b/q_{bc} for all experiments using empirical relationships expressing average impact velocities $\bar{v}_I$ and downstream bedload velocities u_S as a function of depth-averaged flow velocity U_{avg} (Figure 13c; empirical relationship is shown in Figures 6c and 6d) and transport stage τ_{stage} (Figure 13d; empirical relationship shown in Figures 6a and 6b). Prescribed fluxes remain accurately inverted from seismic data for both types of model predictions, although they are more uncertain than inversions using directly measured quantities (Figure 13b), as expected. Inverted sediment fluxes are also more uncertain when empirical relationships for particle transport kinematics are based on τ_{stage} rather than U_{avg} because of the missing slope dependency of impact velocities that is not accounted for in the τ_{stage}-relationships (Figures 6e, 6f and 11e).

Discussion

The complexity of bedload kinematics is characterized by broadly distributed and, on average, shorter than expected times between impacts (Sklar and Dietrich, 2004) under the rough flow conditions of our experiments. This complex behavior is observed for single moving and multiple moving particles and is likely due to highly perturbed flow hydraulics in steep, shallow, and rough streams, which have reduced turbulence intensity and reduced lift forces (Lamb *et al.*, 2017a, 2017b) and perturbed grain saltation trajectories (Huda and Small, 2014). Despite this complexity, the relationships between average quantities that define bedload transport physics (for single moving particles) and flow hydraulics exhibit similar features to those obtained in previous experiments with smoother flow conditions (H is significantly larger than D_{50}; see ; Chatanantavet *et al.*, 2013; Nino *et al.*, 1994; Nino and Garcia, 1998; Francis, 1973; Abbott and Francis, 1977; Hu and Hui, 1996). Times between impacts for single moving particles have a relative dependence on τ_{stage} that is similar to that proposed previously (Sklar and Dietrich, 2004), and the average stream-wise sediment transport velocity u_S scales linearly with the depth-averaged flow velocity U_{avg} and is more a function of U_{avg} than of τ_{stage}, as observed in previous experiments (Chatanantavet *et al.*, 2013). The same is true for the average impact velocity $\bar{v}_I$ oriented normal to the bed roughness (see Figure 1b), which to our knowledge has not been measured previously in such rough flow conditions. $\bar{v}_I$ scales linearly with both U_{avg} and u_S, and is more a function of U_{avg} than of τ_{stage}. This later observation suggests that the variations in the vertical component of the impact velocity $\bar{w}_{inc}$ with changes in transport stage τ_{stage} (Sklar and Dietrich, 2004) only negligibly affect the resultant impact velocity $\bar{v}_I$, and thus that the incident impact velocity v_{inc} has a relatively small angle with respect to the flow direction. Perhaps unexpectedly, though, impact velocity $\bar{v}_I$ is found to be nearly vertical. Incident impact velocities being oriented mostly along flow but impact velocities being nearly vertical can be explained if grains maintain most of their horizontal speed, causing the change in velocity due to impact to mostly be in the upward direction (as shown in Figure 1b). This is still consistent with $\bar{v}_I$ scaling with U_{avg} since v_{inc} (including its vertical component w_{inc}) scales with U_{avg} and $\bar{v}_I$ is simply geometrically related

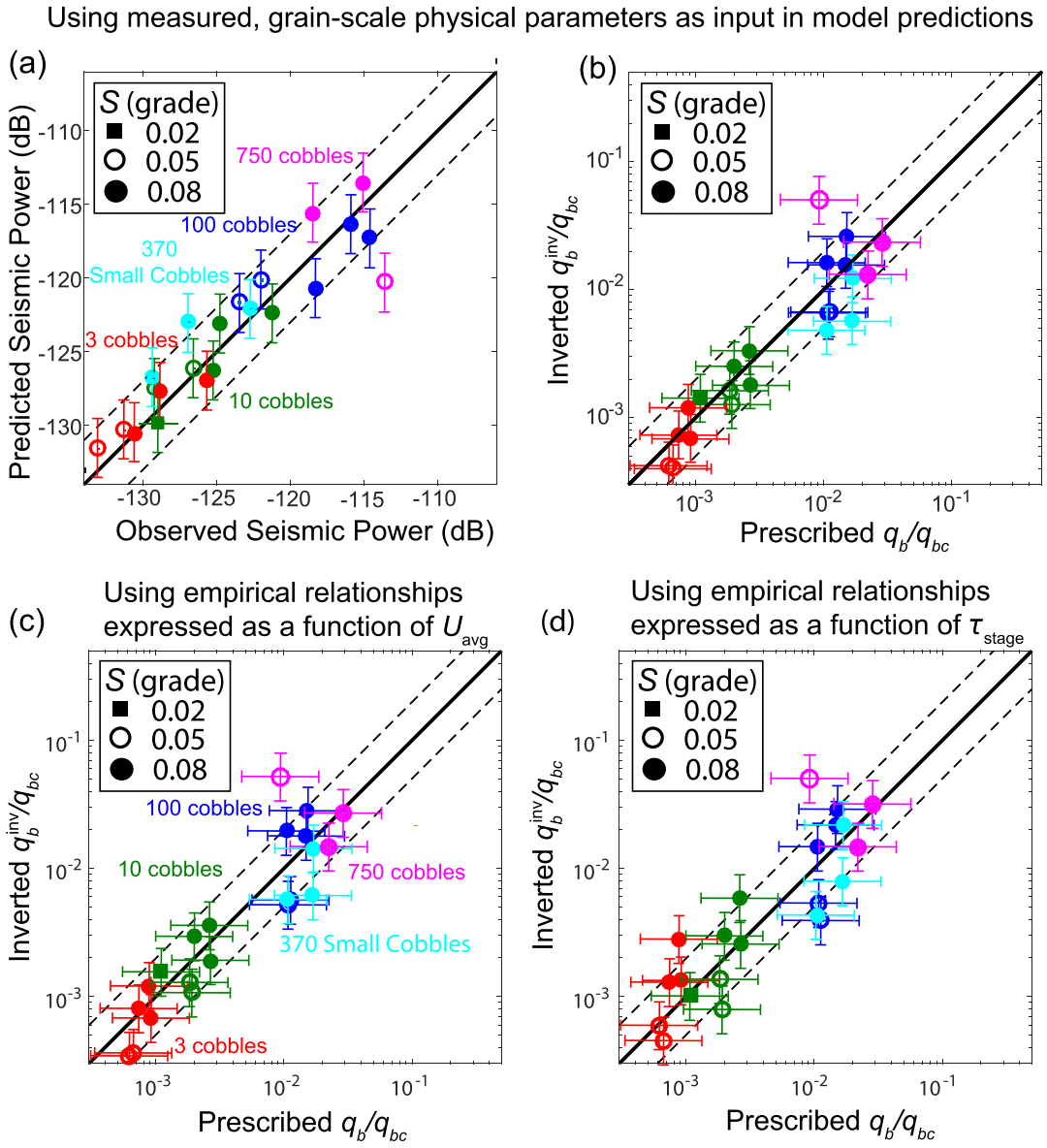

Figure 13. (a) Seismic power predictions versus observations and (b–d) inverted sediment flux versus prescribed sediment flux. Predictions are made using (a, b) measured, grain-scale physical parameters as input and (c, d) empirical relationships expressed as a function of (c) U_{avg} and (d) τ_{stage}. Sediment flux values are normalized by sediment flux at transport capacity, which is calculated as $q_{bc} = 5.7\sqrt{R_g g D_{50}^3}(\tau^*(D_{50}) - \tau_c^*(D_{50}))^{3/2}$ (Fernandez-Luque and van Beek, 1976). Symbols indicate slope (see legends) and colors stand for cobble number. Dashed lines show a factor of two deviations around the one-to-one relationship. [Colour figure can be viewed at wileyonlinelibrary.com]

to v_{inc}. We note, however, that these results could also be because smart rocks are larger than bed grains, and thus may not hold for transported grains that are smaller.

Our experimental findings on bedload kinematics under rough flow support the applicability of the bedload-induced noise framework to seismic observations near mountain rivers. The assumption in previous theory (Tsai *et al.*, 2012) that impacts are oriented normal to the bed remains true for rough bed conditions, such that the use of a Green's function for Rayleigh waves as done in Tsai *et al.* (2012) may be appropriate. In addition, although bedload transport statistics are far more complex than originally accounted for in previous theory (Tsai *et al.*, 2012), the resulting seismic noise characteristics remain mostly unchanged. The broadly distributed but, on average, shorter than expected times between impacts are unlikely to significantly affect seismic noise spectral content, and have effects on seismic noise amplitude that turn out to approximately cancel each other: broadly distributed times between impacts cause about a factor of two decrease in predicted seismic power per impact, but this effect is counterbalanced by higher impact rates and thus seismic power being on average about twice as high. Explicit representation of broadly distributed times between impacts on seismic power may be done by introducing the empirical impact efficiency parameter E_I, defined in our experiments as $E_I \approx 0.6\tau_{stage}^{0.1}$. Simplification of the framework and further improvement of the accuracy of predictions may be done by expressing u_S and $\bar{v}_I$ as a function of U_{avg} instead of τ_{stage}, when good field estimates of U_{avg} are available. Finally, within the range of investigated sediment fluxes, we find that particle–particle interactions occurring at the highest flow rates have negligible effect on seismic power, likely as a result of particle-bed impacts for tests at the highest fluxes being less energetic but more frequent than expected for individually moving particles at lower fluxes, such that the two effects largely cancel out. Interactions between transported particles at the highest fluxes may thus be neglected when applying the bedload-induced noise

framework, although further testing should be conducted with bedload transport conditions near capacity.

Several problems of the bedload-induced noise framework could not be tested in our experiments, and thus motivate further experimental investigations. First, the ground-detached steel flume prevented us from fully testing how bedload impact forces applied on the flume bed convolve with typical Green's functions of the Earth surface. Future experiments made in artificial channels directly coupled to the ground would be useful to tackle this aspect. Furthermore, use of our large flume with fixed cobble bed grains of a given size prevented us from meaningfully testing the framework under a wide range of transported grain sizes, although grain size is known to have major control on seismic power. Future experiments exploring a wider range of grain sizes would nicely complement the present dataset. Finally, and to our view most importantly, use of a fixed cobble bed in our experiments prevented grain exchange between the bed and the bedload, causing uncertainties in our estimates of bedload flux at transport capacity. In our experiments the sediment supply was far lower than the transport capacity, as expected from Fernandez-Luque and van Beek (1976). While limited sediment supply often leads to under-capacity transport in some natural systems, capacity-limited transport is also common in other places. It remains an open question as to how seismic energy would be influenced by much higher transport rates and more mobile bed surfaces. However, our experiments with different sediment loads suggest that additional particle–particle collisions, which would likely be even more important at higher sediment loads, may have little effect on the predicted seismic power because of the offsetting effects of shorter times between collisions and less energetic collisions, as described above.

Monitoring with careful field instrumentation could also be conducted in order to fill the knowledge gaps identified based on our experiments, and to test the modeling framework against observations in natural environments. The deployment of dense arrays near various rivers allowing characterization of the Green's function under different lithologies and topographies would be particularly useful. Measurements of the Green's function in those situations are lacking, and the bedload-induced noise framework relies on a proper, likely site-specific, description of the Green's function. Field observations that range from supply limited to near transport capacity along a single reach of a river would also be useful to constrain the model. For these investigations as well as for any seismological investigation of geomorphological interest in natural streams, one should make sure that good constraints are available on transported grain sizes, since this parameter exerts a primary control on bedload flux inversions that is far greater than any uncertain parametrization related to sediment transport dynamics. More generally, the seismic instrumentation of field sites with highly resolved in-stream measurements of bedload transport and flow turbulence is particularly important if one is to be able to fully test the framework and seismic inversions at the natural scale. This step is essential to fully demonstrate applicability of the framework to sediment management and mitigation applications.

Finally, findings in this study can directly be extrapolated to the prediction of bedload-induced erosion rates. Erosion rate is expected to scale with impact velocities (squared) and rates (linearly) just as seismic power does, such that (i) seismic observations may be used as a proxy for fluvial erosion, and (ii) the present findings are applicable to the prediction of bedload-controlled erosion rates. Broadly distributed but, on average, shorter than expected times between impacts are thus unlikely to significantly change predictions of bedload-induced erosion rates using existing physically based erosion models such as in Sklar and Dietrich (2004), even for situations with multiple moving particles interacting significantly with each other, in which case shorter times between collisions and less energetic collisions may have canceling effects. Predictions of erosion rates could, however, be improved by incorporating an extra bed-slope dependency for cobble velocity u_S and impact velocity $\bar{v}_I$ when expressed as a function of τ_{stage} (see Figures 6e, 6f). This extra bed-slope dependency for u_S and $\bar{v}_I$ could be due to a geometrical effect related to transported grains undergoing more impacts at smaller slopes for rough beds (see Figure 7b), although further experimental work may be required to provide a better understanding of its origin and implications.

Conclusions

We use flume experiments to jointly investigate bedload sediment transport dynamics at the grain scale using smart rocks, and at the channel scale using seismic motion. Based on the smart rock observations, we develop an improved model of bedload-induced seismic noise. Our new model includes (i) a description of impact velocity oriented normal to the bed roughness, instead of only the vertical component of the incident impact velocity as taken as an approximation in previous theory, (ii) time between impacts being, on average, two to three times shorter than commonly expected from saltation theory, and (iii) a description of full distributions of impact hop times and velocities under given flow conditions. Accounting for point (i) in model predictions reduces uncertainties, since impact velocities are found to accurately scale with depth-averaged flow velocities. However, we also find that using previously proposed scaling relationships for impact velocity results in similar predictions since these velocities are similar in magnitude to impact velocities from our new findings. Accounting for point (i) also has little effect on seismic wave generation because Rayleigh waves should mainly be excited by the bedload source due to impact velocities oriented normal to the bed roughness being oriented nearly vertically. The two other points (ii) and (iii) have noticeable effects on the amplitude of seismic power but no effects on its frequency content. Compared to predictions from previous theory, incorporating (ii) causes seismic power to increase by about a factor of two, while incorporating (iii) causes seismic power to decrease by about a factor of two. Thus our final model predictions have predicted seismic power similar to that predicted using previous theory.

Nearly vertical and roughness-normal impact velocities are observed to be a linear function of average downstream cobble velocities, and both velocities show an extra bed-slope dependency that is not represented in existing saltation models. Incorporating these effects into an improved bedload-induced seismic noise model allows sediment flux to be inverted within a factor of two uncertainty. This result holds over a wide range (nearly two orders of magnitude) of prescribed sediment fluxes, and despite significant particle–particle collisions inferred at the higher fluxes. These results support the applicability of the framework to mountain rivers, although further experiments remain to be conducted at fluxes closer to transport capacity.

Acknowledgements—This work was supported by NSF grant EAR-1558479, the Terrestrial Hazard Observation and Reporting Center at the California Institute of Technology and the ANR grant ANR-17-CE01-0008-01. We thank Anne-Sophie Drouet for help in processing the smart rock data, Fanny Brun and Jeff Prancevic for help

in conducting preliminary flume and smart rock experiments, and Bismark Wong for help in inferring sediment flux at high rates from video analysis.

Notation

a Grain acceleration ($m\,s^{-2}$) (see Equation (4))
a_j Component j of smart rock acceleration ($m\,s^{-2}$) (see Equation (4))
C_d Drag coefficient (dimensionless) (see 'Impact velocities and hop times for individual particles')
X Coefficient used for empirical fit with exponential tail (dimensionless) (see 'Impact velocities and hop times for individual particles' and Figure 6)
C_1 Ratio between particle ejection or rise time and particle fall time (dimensionless) (equal to 2/3; see 'Impact velocities and hop times for individual particles')
D Grain diameter (m) (see 'Rationale')
D_{SR} Smart rock intermediate b-axis diameter (m) (equal to 0.09 m; see Figure 2)
D_{NG} Natural grain diameter (m) (see Figure 2)
D_{50} Median grain size (m)
D_{50}^{L} Median grain size of the large grain set (m) (equal to 0.07 m; see Figure 2)
D_{50}^{S} Median grain size of the small grain set and that of the channel fixed bed (m) (equal to 0.045 m; see Figure 2)
e Coefficient of restitution of impact (dimensionless) (see 'Modeling principle and theory of Tsai *et al.* (2012)')
E_I Empirical function that describes the effect of impact full distribution on seismic power (dimensionless) (see 'Extension of the theory to a probabilistic framework with impacts on a rough river bed' and Figure 9)
f Seismic frequency (Hz) (see 'Rationale')
f_{max} Maximum seismic frequency (Hz) (equal to 50 Hz; see 'Bedload-induced seismic noise and comparison to theory')
F Bedload source force function (N) (see Equation (2))
F_2 Vertical bedload source force function (N) (see 'Rationale')
$F_{I,j}$ jth component of the single bedload impact force function (N) (see Equation (3) and 'Extension of the theory to a probabilistic framework with impacts on a rough river bed')
Fr Froude number (dimensionless) (see Table I)
g Acceleration due to gravity ($m\,s^{-2}$) (set to $g = 9.81\ m\,s^{-2}$)
G Green's function ($m\,s^{-1}\,N^{-1}$) (see Equation (2))
G_R Green's function for Rayleigh waves ($m\,s^{-1}\,N^{-1}$) (see 'Modeling principle and theory of Tsai *et al.* (2012)')
$G_{R,2}$ Vertical-to-vertical Green's function for Rayleigh waves ($m\,s^{-1}\,N^{-1}$) (see 'Modeling principle and theory of Tsai *et al.* (2012)')
G_F Flume Green's function ($m\ s^{-1}N^{-1}$) (see 'Experimental strategy to test the models')
$G_{F,2}$ Vertical-to-vertical flume Green's function ($m\,s^{-1}\,N^{-1}$) (see 'Green's function calibration')
$\bar{G}_{F,2}$ Vertical-to-vertical flume Green's function averaged in the bedload, 25–50 Hz frequency range of interest for bedload transport ($m\,s^{-1}\,N^{-1}$) (set to $7.66 \times 10^{-8}\ m\,s^{-1}\,N^{-1}$; see 'Green's function calibration')
H Depth of flow (m) (see Table I)
H_b Bedload height (m) (see Equation (18))
$\hat{H}_b$ Non-dimensional bedload hop height (dimensionless) (see Equation (17))
I Vertical component of the impact impulse ($kg\,m\,s^{-1}$) (see Equation (4))
k_s Roughness length of the river bed (m) (here set to $3D_{50}^{S}$ (Kamphuis, 1974))
L Length over which sediments move (m) (see 'Rationale')
m Grain mass (kg) (see Equation (4))
N Total number of moving grains over length L (dimensionless) (defined under 'Rationale')
N_{SR} Number of smart rocks moving in the channel (dimensionless) (see 'Application of the modeling framework to the experiments')
N_{NG} Number of natural grains moving in the channel (dimensionless) (see 'Application of the modeling framework to the experiments')
N_{SR}^{inv} Inverted number of smart rocks moving in the channel (dimensionless) (see Equation (15))
N_{NG}^{inv} Inverted number of natural grains moving in the channel (dimensionless) (see Equation (15))
N_I Total number of impacts recorded by smart rocks for a given flow configuration (dimensionless) (see 'Impact velocities and hop times for individual particles')
n_D Number of moving grains per unit grain size and per unit channel length (m^{-2}) (see 'Rationale')
$n_I(t_I)$ Average number of impacts occurring during the time interval $[t_i - dt_i/2, t_i + dt_i/2]$ (see 'Impact velocities and hop times for individual particles')
p_D Log-'raised cosine' probability distribution function (per unit grain size, m^{-1}) (see 'Rationale', defined in Tsai et al., 2012)
p_D^L Log-'raised cosine' probability distribution function of the large grain set (per unit grain size, m^{-1}) (see Figure 2)
p_D^S Log-'raised cosine' probability distribution function of the small grain set (per unit grain size, m^{-1}) (see Figure 2)
p_I Probability distribution function of hop times between impacts (per unit time, t^{-1}) (see Equation (5) and Figure 2c)
P Ground seismic velocity power ($m^2\,s^{-2}\ Hz^{-1}$) (see Equation (1))
P^{Tsai} Vertical ground seismic velocity power as predicted from Tsai *et al.* (2012) ($m^2\,s^{-2}\,Hz^{-1}$) (see Equation (3))
P_{D,t_I} Vertical seismic power per unit grain impact, unit grain size and unit length ($m^{-1}\,s^{-2}\,Hz^{-1}$) (see Equation (5))
P_{SR} Vertical flume ground velocity power predicted for smart rocks moving as bedload ($m^2\,s^{-2}\,Hz^{-1}$) (see Equation (11))
P_{NG} Vertical flume ground velocity power predicted for natural grains moving as bedload ($m^2\,s^{-2}\,Hz^{-1}$) (see Equation (13))
P^{obs} Observed vertical flume seismic power averaged in the bedload, 25–50 Hz frequency range ($m^2\,s^{-2}\,Hz^{-1}$) (see Equation (15))
q_b Bedload sediment flux ($m^2\,s^{-1}$) (see 'Rationale')
q_b^{inv} Bedload flux as inverted from noise in our experiments ($m^2\,s^{-1}$) (see Equation (16))
$q_{b,SR}^{inv}$ Smart rock bedload flux as inverted from seismics in our experiments ($m^2\,s^{-1}$) (see Equation (16))
$q_{b,NG}^{inv}$ Natural grains bedload flux as inverted from seismics in our experiments ($m^2\,s^{-1}$) (see Equation (16))
q_{bD} Bedload flux per unit grain size ($m\,s^{-1}$) (see 'Rationale')
q_{bc} Bedload flux at transport capacity ($m^2\,s^{-1}$) (see 'Observed versus predicted absolute seismic power using measured grain kinematics', calculated from Fernandez-Luque and van Beek, 1976)
Q Total flow discharge ($m^3\,s^{-1}$) (see 'Flume setup and flow/sediment transport conditions')
Q_{sub} Subsurface flow discharge ($m^3\,s^{-1}$) (see 'Flume setup and flow/sediment transport conditions')
R Length of river (m) (see Equation (3))
R_g Excess grain density (dimensionless) (see 'Flume setup and flow/sediment transport conditions')

Re_{k_s} Bed roughness Reynolds number (dimensionless) (see 'Flume setup and flow/sediment transport conditions')
S Channel bed slope (grade) (see 'Flume setup and flow/sediment transport conditions')
t Time (s) (see Equation (1))
t_c Contact time of an impact (s) (see Equation (4))
t_l Hop time between impacts (s) (see Equation (5))
T Duration of the time window used to calculate power spectral density (s) (see Equation (1))
u_* Bed shear velocity ($\mathrm{m\,s^{-1}}$) (see 'Flume setup and flow/sediment transport conditions')
U Ground seismic velocity ($\mathrm{m\,s^{-1}}$) (see Equation (1))
u_{inc} Horizontal component of the incident impact velocity ($\mathrm{m\,s^{-1}}$) (see Figure 1)
U_{sub} Subsurface depth averaged velocity ($\mathrm{m\,s^{-1}}$) (see 'Flume setup and flow/sediment transport conditions')
U_{avg} Depth-averaged flow velocity ($\mathrm{m\,s^{-1}}$), excluding subsurface flow (see 'Flume setup and flow/sediment transport conditions)'
$U_{\mathrm{avg},c}$ Critical depth averaged flow velocity for grain motion (see 'Impact velocities and hop times for individual particles' and Figure 6)
u_S Average stream-wise bedload velocity ($\mathrm{m\,s^{-1}}$) (see 'Rationale')
V Grain volume ($\mathrm{m^3}$) (see 'Rationale')
V_{SR} Smart rock volume ($\mathrm{m^3}$) (see Equation (11))
V_{NG} Natural grain volume ($\mathrm{m^3}$) (see Equation (13))
v_I Impact velocity as measured from the smart rock, i.e. impact velocity normal to bed roughness ($\mathrm{m\,s^{-1}}$) (see 'Particle transport kinematics from smart rocks' and Figure 1)
$v_{I,j}$ Component j of the impact velocity oriented normal to bed roughness ($\mathrm{m\,s^{-1}}$) (see Figure 1)
v_{inc} Incident impact velocity ($\mathrm{m\,s^{-1}}$) (see Figure 1)
v_{out} Reflected impact velocity ($\mathrm{m\,s^{-1}}$) (see Figure 1)
W River width (m) (equals 1 m in our experiments; see 'Flume setup and flow/sediment transport conditions')
w_{inc} Vertical incident impact velocity ($\mathrm{m\,s^{-1}}$) (see Equation (4) and Figure 1)
w_{ref} Vertical reflected impact velocity ($\mathrm{m\,s^{-1}}$) (see Equation (4))
$w_{\mathrm{inc}}^{\mathrm{drop}}$ Vertical incident impact velocity in cobble drop calibration experiments ($\mathrm{m\,s^{-1}}$) (see 'Flume setup and flow/sediment transport conditions')
$w_{\mathrm{ref}}^{\mathrm{drop}}$ Vertical reflected impact velocity in cobble drop calibration experiments ($\mathrm{m\,s^{-1}}$) (see 'Flume setup and flow/sediment transport conditions')
w_s Average settling velocity ($\mathrm{m\,s^{-1}}$) (see Equation (23))
w_{st} Terminal grain settling velocity ($\mathrm{m\,s^{-1}}$) (see Equation (17))
$\mathbf{x}_0$ Reference coordinate vector of a given grain within the channel (m) (see Equation (2))
$\mathbf{x}$ Reference coordinate vector of the seismic station (m) (see Equation (1))
z Elevation above the bed (m) (see Figure 1)
z^{drop} Height used for grain drop calibration experiments (m) (see 'Experimental Strategy, Methods and Measurements)
α Exponent for extrapolation of critical Shields stress to various grain sizes (dimensionless) (equal to 0.9; see 'Flume setup and flow/sediment transport conditions')
δv Velocity variation due to an impact ($\mathrm{m\,s^{-1}}$) (see 'Particle transport kinematics from smart rocks')
η Thickness of the subsurface layer (m) (see 'Flume setup and flow/sediment transport conditions')
γ Coefficient that expresses inelastic energy dissipation during impact (dimensionless) (see Equation (4))
ν Water kinematic viscosity ($\mathrm{m^2\,s^{-1}}$) (see 'Flume setup and flow/sediment transport conditions')
ρ Water density ($\mathrm{kg\,m^{-3}}$) (equal to 1000 $\mathrm{kg\,m^{-3}}$; see 'Flume setup and flow/sediment transport conditions')
ρ_s Grain density ($\mathrm{kg\,m^{-3}}$) (equal to 2600 $\mathrm{kg\,m^{-3}}$; see 'Flume setup and flow/sediment transport conditions')
σ Standard deviation of the equivalent normal distribution of the log-'raised cosine' distribution (dimensionless) (equal to 0.12; see 'Flume setup and flow/sediment transport conditions' and Tsai et al., 2012)
τ_b Bed shear stress ($\mathrm{N\,m^{-2}}$)
τ_{stage} Transport stage (dimensionless) (see 'Flume setup and flow/sediment transport conditions')
τ^* Shields stress (dimensionless) (see 'Flume setup and flow/sediment transport conditions')
τ_c^* Critical value of Shields stress (dimensionless) (see 'Flume setup and flow/sediment transport conditions')
$\tau_{c,\mathrm{SR}}^*$ Critical value of Shields stress for smart rocks (dimensionless) (see 'Flume setup and flow/sediment transport conditions')
$\tau_{c,\mathrm{NG}}^*$ Critical value of Shields stress for natural grains (dimensionless) (see 'Flume setup and flow/sediment transport conditions')
θ River slope angle (°) (see 'Impact velocities and hop times for individual particles')
Θ_I Impact angle relative to vertical (°) (see Figures 1b and 7)
Θ_{inc} Incident impact angle relative to horizontal (°) (see Figure 1b)
Θ_{mod} Modified impact angle once corrected from the local bed surface slope (°) (see Figure 1b)
ξ Fraction of smart rocks versus natural grains moving in the channel (dimensionless) (see 'Application of the modeling framework to the experiments')

Appendix A : Critical Shields Stress Estimates from Dry Friction Experiments and Empirical Modeling

The dry friction angle was obtained from tilt-table experiments in which a smart rock was deposited on a small-scale replica of the flume cobble bed (the bed was made of grain sizes similar to those in the large-scale flume), which then was tilted

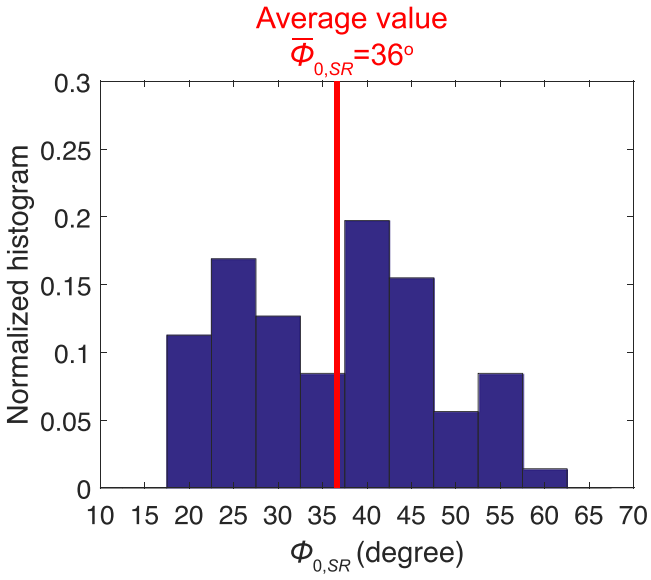

Figure A.1. Normalized histogram of smart rock dry friction angle values obtained from tilt-table experiments. The red vertical line indicates the average value of 36° used to calculate critical Shields stress. [Colour figure can be viewed at wileyonlinelibrary.com]

progressively until the smart rock was dislodged and fell down (Miller and Byrne, 1966). The critical angle for smart rock motion was recorded, and this procedure was repeated 70 times. The probability density function of all friction angles is shown as a histogram in Figure A.1. We found an average friction angle of ϕ_0=36°±11°, where 11° corresponds to 1 sigma. This value is relatively low compared to those previously found in other studies (e.g. 41–59° in Prancevic and Lamb, 2015). This may be explained by smart rocks being bigger than the relatively densely packed rocks glued to the bed, such that the smart rock is often sitting on top of the bed roughness and therefore offers little frictional resistance.

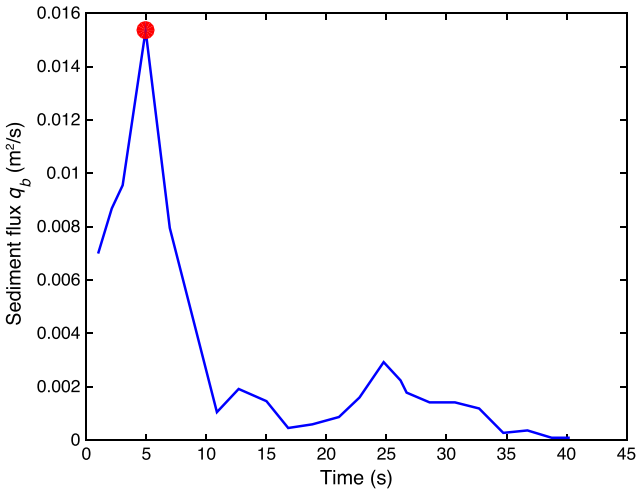

Figure A.2. Time series of sediment flux q_b obtained from counting pebbles using overhead high-rate videos. The blue line shows measurements conducted every 2 s, and the red dot shows the maximum sediment flux value that is compared with maximum recorded seismic power (see red dots in Figure 3b). [Colour figure can be viewed at wileyonlinelibrary.com]

We converted the dry friction angle found from the tilt-table experiments into critical Shields stress values by using the average and fluctuating flow velocities of the hydraulic model of Lamb *et al.* (2008b) with zero form drag. Using smart rock diameter D_{SR} = 9 cm, setting bed roughness k_s equal to median grain size D_{50} = 4.5 cm and neglecting morphological form drag as well as wall shear stress, we predict $\tau^*_{c,SR}$ to be equal to 0.0210, 0.0315 and 0.0451 for our investigated slopes of 0.02, 0.05 and 0.08 grades, respectively.

Appendix B : Bedload Sediment Flux Calculations

At low and intermediate sediment fluxes (with 1–350 cobbles)

We relate the number of grains N moving in the channel with sediment flux q_b a posteriori by assuming that all grains are uniformly distributed over length L of the sediment pulse and across the width W of the channel. Under this assumption, N is related to the number of grains n_D per unit grain size and per unit pulse length as

$$N = \frac{Ln_D(D)}{p_D(D)} \tag{A.1}$$

where $p_D(D)$ is the grain size distribution function (per unit grain size) and n_D relates to sediment flux as (see also main text, 'Rationale')

$$n_D = \frac{Wq_{bD}}{Vu_S}. \tag{A.2}$$

Substituting the definition of n_D in Equation (A.2) into the definition of N in Equation (A.1), we find that q_b depends on N as

$$q_b = \frac{Nu_S}{\mathrm{WL}} \int_D p_D V(D) \mathrm{d}D. \tag{A.3}$$

Equation (A.3) is used in the main text to calculate the sediment flux $q_{b,\mathrm{NG}}$ of N_{NG} natural grains with various diameters

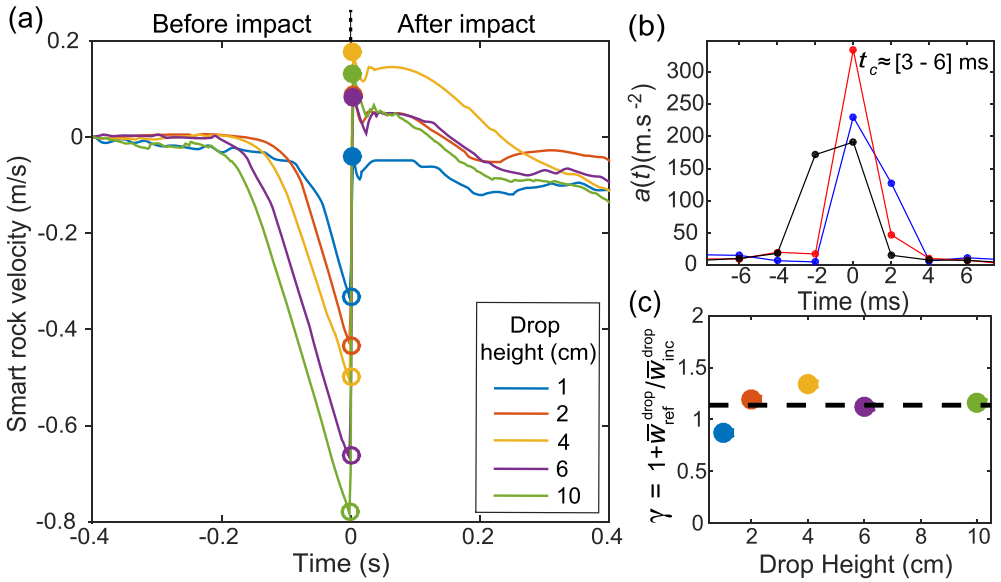

Figure A.3. Linking smart rock acceleration records with impact characteristics from submerged smart rock drop experiments. (a) Average smart rock velocity time series obtained from time integrating the smart rock acceleration records around each impact of a given drop height. Empty circles highlight impact incident velocities $\bar{w}^{drop}_{inc}$ and filled circles highlight impact reflected velocities $\bar{w}^{drop}_{ref}$. Red dots indicate acceleration maxima automatically picked for each impact. (b) Zoom on smart rock acceleration records for three arbitrarily selected impacts of the 4 cm drop height experiments shown in Figure 1a. (c) γ-values obtained from the impact velocity changes shown in (c) (see Equation (4)). The dashed line indicates the average γ-value of 1.13. [Colour figure can be viewed at wileyonlinelibrary.com]

(Figure 2c). A simpler form is obtained for sediment flux $q_{b,SR}$ of N_{SR} smart rock since those all have approximately the same diameter, in which case $p_D(D)$ for smart rocks is a Dirac delta function (Figure 4.2.1) and we have $q_{b,SR} = N_{SR}\frac{u_S V_{SR}}{WL}$. Total sediment flux q_b for each experiment is then calculated as $q_b = q_{b,NG} + q_{b,SR}$.

At the highest sediment fluxes (with 750 cobbles)

For the high sediment flux rates of experiments with 750 cobbles, we infer sediment flux using overhead videos taken in the middle range of the flume test section. Using these videos, we manually counted the number of cobbles N_t that crossed a given line (colocated with the seismometer) over a given time window (using a 2 s time window to match that used to calculate power from the seismic record). Sediment flux at time t is calculated as $q_{b,t} = \frac{N_t}{WT}\int_D p_D(D)V(D)dD$, and is shown in Figure A.2 for the experiment at 0.08 grade slope and 392 $l s^{-1}$ discharge (see Table II). The maximum value of sediment flux (highlighted by the red dot) is then used to compare with the maximum recorded seismic power (see red dots in Figure 4b).

Appendix C : Using Calibrated Smart Rock Records to Infer Impact Velocities During Sediment Transport

Smart rock calibration

Smart rocks impacted the flume cobble bed after a free fall from a given height and with small enough rotation that velocity time series can be reconstructed by integrating the vertical acceleration time series over the impact time. Eighty drops were performed at heights from 1 to 10 cm above the cobble of the bed. All spikes observed in the smart rock acceleration record match impacts (Figure 3b). Thus the 512 Hz smart rock sampling rate is high enough to detect every impact, although it is insufficient to resolve the details of the acceleration time series during the impact because impacts are detected over only two to three measurement points (Figure A.3a). Maximum

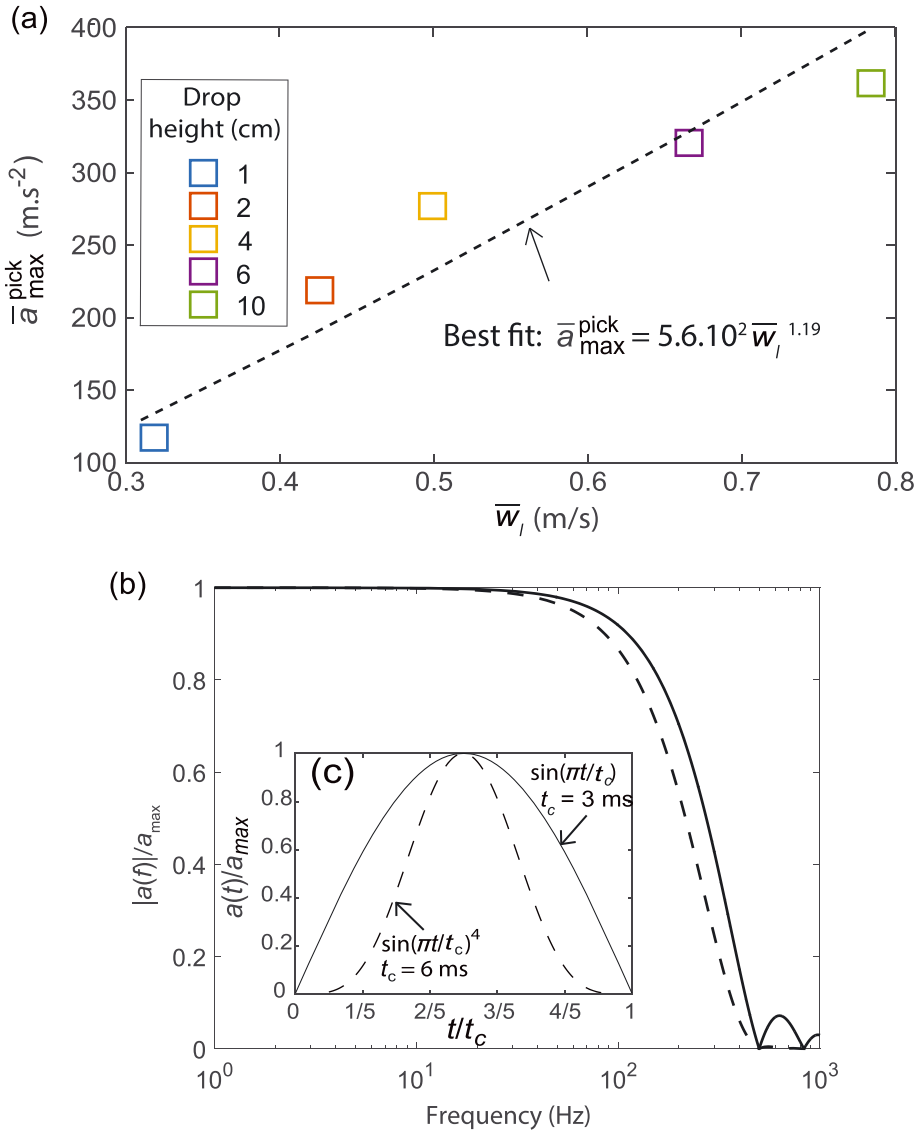

Figure A.4. Comparing smart rock records with expected impact source functions. (a) Maximum picked impact acceleration $\bar{a}^{pick}_{max}$ as a function of average incident impact velocity $\bar{w}_{inc}$. (b, c) Impact acceleration function in the (b) frequency and (c) time domain as inferred from $\int_{t=0}^{t_c} a(t) = I$, where I is obtained independently from trajectory reconstruction (Figure A.3) and $a(t)$ is assumed to be of the form $a(t) = a_{max}\sin(\pi t/t_c)^\beta$ with $\beta = 4; t_c = 6$ ms (dashed lines) and $\beta = 1; t_c = 3$ ms (solid lines). [Colour figure can be viewed at wileyonlinelibrary.com]

acceleration values during impacts as well as impact contact times are consistent with those expected from Hertzian theory (see next subsection), which gives us confidence in the acceleration magnitudes measured with smart rocks. Velocity time series from before and after the impact are calculated for each drop experiment and then averaged together using the impact time as the origin time (Figure A.3a). For each average velocity time series of a given drop height, we calculate $\gamma = 1 + |\bar{w}_{ref}^{drop} / \bar{w}_{inc}^{drop}|$ (Equation (4)) by picking the average incident (negative) velocity $\bar{w}_{inc}^{drop}$ and the average reflected (positive) velocity $\bar{w}_{ref}^{drop}$ (see colored circles). γ is height independent and exhibits an average value of 1.13 (Figure A.3c).

Consistency with Hertz's theory

Averaging maximum smart rock acceleration values $\bar{a}_{max}^{pick}$ (Figure A.4a), we find that $\bar{a}_{max}^{pick}$ scales with incident velocity $\bar{w}_{inc}^{drop}$ to the power 1.19, i.e. roughly to the power 5/4 as expected from Hertz's theory (Farin *et al.*, 2015). Our smart rock measurements are also consistent with the impact acceleration function being of the form $a(t) = a_{max} \sin(\pi t / t_c)^{\beta}$, where β is a given exponent. Using values of t_c ranging from 3 ms for $\beta = 1$ to 6 ms for $\beta = 6$ (Figure A.4c) allows us to verify the condition $\int_{t=0}^{t_c} a(t) = I$, where I is obtained independently (Figure A.3). We thus conclude that our smart rock measurements are consistent with typical impact acceleration functions described in the literature (e.g. Hunter,1957). We are unable, however, to discriminate the exact values of t_c and β, though we note that uncertainties on these parameters do not significantly affect seismic energy in the frequency range of interest (below 50 Hz, Figure A.4b).

Calculation of impact velocities during transport

Impact velocity v_I for bedload transport experiments was obtained by (i) picking impact-induced spikes in the acceleration magnitude time series calculated as $a(t) = \sqrt{\sum_{j=1}^{3} a_j(t)^2}$, where a_j is acceleration along component j (see Figure A.3d); (ii) calculating the velocity variation $\delta v = v_I + v_R$ (where v_R is the reflected impact velocity normal to the bed roughness) for each impact by integrating $a(t)$ over the three measurement points from before and after the impact; and (iii) calculating the impact velocity v_I as $v_I = \delta v / \gamma$ using $\gamma = 1.13$ as found in the calibration experiments presented under 'Impact mechanics of smart rocks'.

Appendix D : Interpretation of the seismic records

Spectral and temporal signature

Seismic power decreases with frequency whether or not bedload occurs in the channel. This spectral signature in the seismic record is partly due to flume resonance preferentially enhancing low frequencies and partly to laboratory water pumps preferentially generating noise at low frequencies (<25 Hz). Those times when sediments were poured into the channel are characterized by high, short-lived seismic power levels (see dashed lines in Figure 4) caused by cobbles strongly impacting the channel bed after having been manually dumped from 50 cm above the bed. Seismic power then increases steadily though time as cobbles are progressively entrained by the flow, and reach a maximum when most cobbles are simultaneously in motion (see solid lines in Figure 4) before it decreases again as cobbles leave the test section and come to rest in the end box.

Definition of the Green's function

Substituting the definition of ground velocity $U(f)$ (Equation (1)) into the definition of seismic power $P(f)$ (Equation (2)), we express the vertical-to-vertical velocity Green's function $G_{F,2}(f)$ for a given impact as $G_{F,2}(f) = \sqrt{T \cdot P(f) / F_{I,2}(f)^2}$ where $P(f)$ is the seismic power calculated from the seismogram of duration T resulting from the impact, and $F_{I,2}$ is the impact source force defined as $F_{I,2} = I = \gamma m w_{inc}^{drop}$ (Equation (4)). We calculate a reference Green's function $G_{F,2}(f)$ using $T = 2$ s for a reference impact nearby the seismometer (see black dot in Figure 5) using $w_{inc}^{drop} = \sqrt{2gz^{drop}}$ and $\gamma = 1.13$ as found under 'Impact mechanics of smart rocks' (Figure A.5). In the frequency range of interest for bedload, we obtain $\bar{G}_{F,2}(25 < f < 50) = 7.66 \times 10^{-8}$ m s^{-1}/N. Using this measurement, we assume that the impact used for cali-

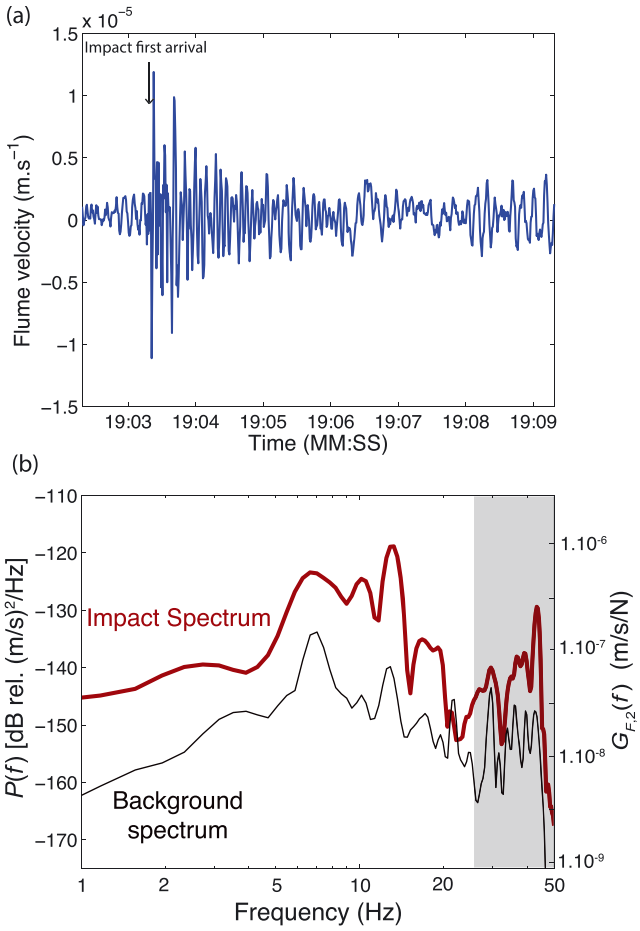

Figure A.5. Definition of the reference Green's function from a cobble impact conducted at the location indicated by the black dot in Figure 5. (a) Seismic ground velocity time series including waves due to the impact and (b) seismic power associated with the impact (thick red) and with background noise (thin black). Since impact force spectrum is flat, the red line also corresponds to the Green's function with associated values shown on the right y-axis. The gray area shows the bedload frequency range in which the Green's function is averaged to conduct model predictions. [Colour figure can be viewed at wileyonlinelibrary.com]

bration is instantaneous relative to the seismic sampling time, and that the parameter γ as inferred previously in resting water is similar in air. The former assumption is supported by the time of impact in air being shorter than that in water, which has already been shown to be instantaneous relative to the 25–50 Hz seismic sampling frequency of interest ('Impact mechanics of smart rocks'). The latter assumption is supported by the fact that the Stokes number is of the order of 10^3 or larger for impacts in water or air, respectively, and that for these high Stokes numbers the surrounding fluid is not expected to significantly affect γ (Gondret *et al.*, 2002).

References

Abbott JE, Francis JRD. 1977. Saltation and suspension trajectories of solid grains in a water stream. *Philosophical Transactions of the Royal Society of London A* **284**(1321): 225–254.

Aki K, Richards PG. 2002. *Quantitative Seismology*, 2nd ed. University Science: Sausalito, CA.

Burtin A, Bollinger L, Vergne J, Cattin R, Nábalek JL. 2008. Spectral analysis of seismic noise induced by rivers: A new tool to monitor spatiotemporal changes in stream hydrodynamics. *Journal of Geophysical Research: Solid Earth* **113**(B5): B05301.

Burtin A, Cattin R, Bollinger L, Vergne J, Steer P, Robert A, Findling N, Tiberi C. 2011. Towards the hydrologic and bed load monitoring from high-frequency seismic noise in a braided river: The torrent de St Pierre, French Alps. *Journal of Hydrology* **408**(1–2): 43–53.

Chao W-A, Wu Y-M, Zhao L, Tsai VC, Chen C-H. 2015. Seismologically determined bedload flux during the typhoon season. Scientific Reports 5. Available: http://www.nature.com/srep/2015/150205/srep08261/full/srep08261.html [16 September 2018].

Chatanantavet P, Whipple KX, Adams MA, Lamb MP. 2013. Experimental study on coarse grain saltation dynamics in bedrock channels. *Journal of Geophysical Research: Earth Surface* **118**(2): 1161–1176.

Cook KL, Turowski JM, Hovius N. 2013. A demonstration of the importance of bedload transport for fluvial bedrock erosion and knickpoint propagation. *Earth Surface Processes and Landforms* **38**(7): 683–695.

Cook KL, Andermann C, Gimbert F, Adhikari BR, Hovius N. 2018. Glacial lake outburst floods as drivers of fluvial erosion in the Himalaya. *Science* **362**(6410): 53–57.

Díaz J, Ruíz M, Crescentini L, Amoruso A, Gallart J. 2014. Seismic monitoring of an alpine mountain river. *Journal of Geophysical Research: Solid Earth* **119**(4): 3276–3289.

Dietrich WE. 1982. Settling velocity of natural particles. *Water Resources Research* **18**(6): 1615–1626.

Durda DD, Movshovitz N, Richardson DC, Asphaug E, Morgan A, Rawlings AR, Vest C. 2011. Experimental determination of the coefficient of restitution for meter-scale granite spheres. *Icarus* **211**(1): 849–855.

Farin M, Mangeney A, Toussaint R, de Rosny J, Shapiro N, Dewez T, Hibert C, Mathon C, Sedan O, Berger F. 2015. Characterization of rockfalls from seismic signal: Insights from laboratory experiments. *Journal of Geophysical Research: Solid Earth* **120**(10): 7102–7137.

Fernandez-Luque R, van Beek R. 1976. Erosion and transport of bedload sediment. *Journal of Hydraulic Research* **14**(2): 127–144.

Francis JRD. 1973. Experiments on the motion of solitary grains along the bed of a water-stream. *Proceedings of the Royal Society of London A* **332**(1591): 443–471.

Garcia C, Laronne JB, Sala M. 2000. Continuous monitoring of bedload flux in a mountain gravel-bed river. *Geomorphology* **34**(1–2): 23–31.

Gimbert F, Tsai VC, Lamb MP. 2014. A physical model for seismic noise generation by turbulent flow in rivers. *Journal of Geophysical Research: Earth Surface* **119**: 2209–2238.

Gimbert F, Tsai VC, Amundson JM, Bartholomaus TC, Walter JI. 2016. Subseasonal changes observed in subglacial channel pressure, size, and sediment transport. *Geophysical Research Letters* **43**. http//doi.org/10.1002/2016GL068337.

Gondret P, Lance M, Petit L. 2002. Bouncing motion of spherical particles in fluids. *Physics of Fluids* **14**(2): 643–652.

Govi M, Maraga F, Moia F. 1993. Seismic detectors for continuous bed load monitoring in a gravel stream. *Hydrological Sciences Journal* **38**(2): 123–132.

Hsu L, Finnegan NJ, Brodsky EE. 2011. A seismic signature of river bedload transport during storm events. *Geophysical Research Letters* **38**(13): L13407.

Hu C, Hui Y. 1996. Bed-load transport. I. Mechanical characteristics. *Journal of Hydraulic Engineering* **122**(5): 245–254.

Huda SA, Small EE. 2014. Modeling the effects of bed topography on fluvial bedrock erosion by saltating bed load. *Journal of Geophysical Research: Earth Surface* **119**(6): 1222–1239.

Hunter SC. 1957. Energy absorbed by elastic waves during impact. *Journal of the Mechanics and Physics of Solids* **5**(3): 162–171.

Jackson RL, Green I, Marghitu DB. 2010. Predicting the coefficient of restitution of impacting elastic-perfectly plastic spheres. *Nonlinear Dynamics* **60**(3): 217–229.

Kamphuis JW. 1974. Determination of sand roughness for fixed beds. *Journal of Hydraulic Research* **12**(2): 193–203.

Lajeunesse E, Malverti L, Charru F. 2010. Bed load transport in turbulent flow at the grain scale: Experiments and modeling. *Journal of Geophysical Research: Earth Surface* **115**(F4): F04001.

Lamb M, Brun F, Fuller BM. 2017a. Direct measurements of lift and drag on shallowly submerged cobbles in steep streams: Implications for flow resistance and sediment transport. *Water Resources Research* **53**(9): 7607–7629.

Lamb MP, Brun F, Fuller BM. 2017b. Hydrodynamics of steep streams with planar coarse-grained beds: Turbulence, flow resistance, and implications for sediment transport. *Water Resources Research* **53**(3): 2240–2263.

Lamb MP, Dietrich WE, Sklar LS. 2008a. A model for fluvial bedrock incision by impacting suspended and bed load sediment. *Journal of Geophysical Research: Earth Surface* **113**(F3): F03025.

Lamb MP, Dietrich WE, Venditti JG. 2008b. Is the critical shields stress for incipient sediment motion dependent on channel-bed slope? *Journal of Geophysical Research: Earth Surface* **113**(F2): F02008.

Lamb MP, Finnegan NJ, Scheingross JS, Sklar LS. 2015. New insights into the mechanics of fluvial bedrock erosion through flume experiments and theory. *Geomorphology* **244**: 33–55.

Miller RL, Byrne RJ. 1966. The angle of repose for a single grain on a fixed rough bed. *Sedimentology* **6**(4): 303–314.

Nino Y, Garcia M. 1998. Using Lagrangian particle saltation observations for bedload sediment transport modelling. *Hydrological Processes* **12**(8): 1197–1218.

Nino Y, Garcia M, Ayala L. 1994. Gravel saltation. 1. experiments. *Water Resources Research* **30**(6): 1907–1914.

Olinde L, Johnson JPL. 2015. Using RFID and accelerometer-embedded tracers to measure probabilities of bed load transport, step lengths, and rest times in a mountain stream. *Water Resources Research* **51**(9): 7572–7589.

Parker G. 1990. Surface-based bedload transport relation for gravel rivers. *Journal of Hydraulic Research* **28**(4): 417–436.

Prancevic JP, Lamb MP, Fuller B. 2014. Incipient sediment motion across the river to debris-flow transition. *Geology* **42**(3): 191–194.

Prancevic JP, Lamb MP. 2015. Unraveling bed slope from relative roughness in initial sediment motion. *Journal of Geophysical Research: Earth Surface* **120**(3): 2014JF003323.

Rickenmann D, Turowski JM, Fritschi B, Klaiber A, Ludwig A. 2012. Bedload transport measurements at the Erlenbach stream with geophones and automated basket samplers. *Earth Surface Processes and Landforms* **37**(9): 1000–1011.

Roth DL, Finnegan NJ, Brodsky EE, Cook KL, Stark CP, Wang HW. 2014. Migration of a coarse fluvial sediment pulse detected by hysteresis in bedload generated seismic waves. *Earth and Planetary Science Letters* **404**: 144–153.

Roth D, Finnegan N, Brodsky E, Rickenmann D, Turowski J, Badoux A, Gimbert F. 2017. Bedload transport and boundary roughness changes as competing causes of hysteresis in the relationship between seismic shaking and river stage. *Journal of Geophysical Research* **122**: 1182–1200.

Schmandt B, Aster RC, Scherler D, Tsai VC, Karlstrom K. 2013. Multiple fluvial processes detected by riverside seismic and infrasound monitoring of a controlled flood in the Grand Canyon. *Geophysical Research Letters* **40**(18): 4858–4863.

Schmandt B, Gaeuman D, Stewart R, Hansen SM, Tsai VC, Smith J. 2017. Seismic array constraints on reach-scale bedload transport. *Geology* **45**(4): 299–302.

Sklar LS, Dietrich WE. 2004. A mechanistic model for river incision into bedrock by saltating bed load. *Water Resources Research* **40**(6): W06301.

Tsai VC, Minchew B, Lamb MP, Ampuero J-P. 2012. A physical model for seismic noise generation from sediment transport in rivers. *Geophysical Research Letters* **39**(2): L02404.

Welch PD. 1967. The use of fast Fourier transform for the estimation of power spectra: A method based on time averaging over short, modified periodograms. *IEEE Transactions on Audio and Electroacoustics* **15**(2): 70–73.

Whipple KX, Hancock GS, Anderson RS. 2000. River incision into bedrock: Mechanics and relative efficacy of plucking, abrasion, and cavitation. *Geological Society of America Bulletin* **112**(3): 490–503.